Colloquium: Cluster growth on surfaces: Densities, size distributions, and morphologies

Mario Einax*

Fachbereich Physik, Universität Osnabrück, Barbarastraße 7, 49076 Osnabrück, Germany

Wolfgang Dieterich†

Fachbereich Physik, Universität Konstanz, 78457 Konstanz, Germany

Philipp Maass‡

Fachbereich Physik, Universität Osnabrück, Barbarastraße 7, 49076 Osnabrück, Germany

(published 8 July 2013)

Understanding and control of cluster and thin-film growth on solid surfaces is a subject of intensive research to develop nanomaterials with new physical properties. In this Colloquium a review of basic theoretical concepts to describe submonolayer growth kinetics under nonequilibrium conditions is given. It is shown how these concepts can be extended and further developed to treat self-organized cluster formation in material systems of current interest, such as nanoalloys and molecular clusters in organic thin-film growth. The presentation is focused on ideal flat surfaces to limit the scope and to discuss key ideas in a transparent way. Open experimental and theoretical challenges are pointed out.

DOI: 10.1103/RevModPhys.85.921 PACS numbers: 81.15.Aa, 68.55.−a, 68.65.Pq, 75.75.−c

CONTENTS

I. INTRODUCTION

A widely applied method for the design of materials with nanoscale dimensions is to deposit atoms or molecules on a solid substrate. Adsorbed atoms diffuse along the surface, nucleate, and form aggregates. The interplay of these processes leads to a rich variety of self-organized growth phenomena. Nanoscale structures built in this way in general are *metastable*, so that their physical properties can differ distinctly from the corresponding equilibrium bulk phases. Owing to the progress in experimental techniques, especially scanning tunneling microscopy (STM) and atomic force microscopy (AFM), it is possible to uncover microscopic details in the underlying structure formation with unprecedented precision.

Starting out with the pioneering work by Venables and coworkers (Venables, 1973; Venables, Spiller, and Hanbücken, 1984) important theoretical concepts were developed in the past. Today the adatom kinetics of single-component metallic systems is rather well understood. From scaling properties of measured island densities and shapes important kinetic parameters can be extracted, such as adatom diffusion coefficients and interaction energies, sizes of critical nuclei, step edge barriers for interlayer transport, etc. Knowledge of these parameters makes it possible to control the desired growth modes to a substantial degree. Several extensive review articles give an excellent account of the state of the art (Brune, 1998; Ratsch and Venables, 2003; Michely and Krug, 2004; Evans, Thiel, and Bartelt, 2006).

This Colloquium is motivated by the fact that many of the basic questions in the field of surface growth appear nowadays in a new context. This includes self-organized growth of *nanoalloys*, which can show unexpected physical properties emerging from frozen-in nonequilibrium atomic arrangements. The submonolayer regime of alloy growth offers a wealth of new problems relative to growth in one-component adatom systems. Other examples of wide current interest are epitaxial growth of colloids (Einstein and Stasevich, 2010; Ganapathy *et al.*, 2010), growth of graphene on metal substrates (Loginova *et al.*, 2008; Coraux *et al.*, 2009; Zangwill

*mario.einax@uni-osnabrueck.de
†wolfgang.dieterich@uni-konstanz.de
‡philipp.maass@uni-osnabrueck.de

and Vvedensky, 2011), and growth of metallic nanoparticles on graphene (Zhou, Gao, and Goodman, 2010; Pandey *et al.*, 2011; Moldovan *et al.*, 2012). While theoretical treatments of the growth kinetics for these systems are still rare, the general concepts, presented here, can be adapted and refined in order to understand the graphene and nanoparticle formation.

A further important problem is the self-organized growth of *organic molecules* on an inorganic substrate (Kowarik, Gerlach, and Schreiber, 2008; Kühnle, 2009; Hlawacek and Teichert, 2013; Rahe *et al.*, 2013). In the latter case, the complexity of building blocks, provided by organic chemistry, can be exploited for generating an even richer spectrum of surface structures. Such studies are largely driven by perspectives of molecular electronics (Nitzan and Ratner, 2003; Cuniberti, Fagas, and Richter, 2005; Cuevas and Scheer, 2010) and organic photovoltaics (Deibel and Dyakonov, 2010; Nicholson and Castro, 2010).

A challenge in this area is to clarify how far concepts based on single atom surface kinetics remain valid, or require modification when dealing with the larger sizes, potential nonspherical shapes, and internal degrees of freedom of the molecules. Such questions were addressed in recent experiments, but our understanding of mechanisms underlying organic surface growth is just at the beginning. Of particular relevance is to explain which type of island morphologies develop and how they can be controlled. Organic molecules exhibit often only weak interactions with the substrate. As a consequence, dewetting is often observed in molecular pattern formation (Burke, Topple, and Grütter, 2009). Examples are pentacene on SiO_2 (Käfer, Wöll, and Witte, 2009), perylene tetracarboxylic dianhydride (PTCDA) on NaCl (Burke *et al.*, 2008), or C_{60} on KBr (Burke *et al.*, 2005), on NaCl (Burke *et al.*, 2007), and on CaF_2 (Loske *et al.*, 2010). Finally, we note that even the standard theories of cluster growth in monocomponent atomic systems still imply basic, partly long-standing open problems and we point out a few of them.

Our focus is on a set of general questions, which seemingly are well understood but indeed call for a more general treatment or deeper analysis: (i) How many islands form? (ii) What is the distribution of island sizes? (iii) When do islands survive upon continued deposition? (iv) What determines the outer shape and inner structure of clusters? The first two questions are specially important for submonolayer growth and the following ones for multilayer growth. Without reviewing in any detail the current knowledge about these questions, our attention in each case is concentrated on specific open problems which are behind them. Steps toward their solution are proposed, corroborated by simple model studies.

II. ELEMENTARY PROCESSES AND RATE EQUATIONS

Advanced computer simulation techniques have made it possible to study the growth of clusters and films on surfaces in great detail [for a recent review, see Clancy (2011)]. Classical methods such as molecular dynamics (Rapaport, 2004) and kinetic Monte Carlo (KMC) simulations (Landau and Binder, 2005) can nowadays be supported by *ab initio* calculations, which provide precise force fields and/or microscopic parameters entering rates for elementary jump processes. Such approaches (Kratzer and Scheffler, 2001) are important to account for specifics of material systems. To capture long time and length scales in the growth kinetics, continuum phase-field models have been developed, where atomic features are resolved up to a certain extent (Provatas and Elder, 2010). Prominent approaches are the level set method (Gyure *et al.*, 1998; Ratsch and Venables, 2003) and the phase-field crystal method (Elder *et al.*, 2002; Greenwood, Provatas, and Rottler, 2010). The latter is based on a modulated density field that minimizes a free energy functional. Construction of this functional to adequately describe patterning in ultrathin films is the major challenge of the phase-field crystal method (Elder *et al.*, 2012).

To bring up the basic principles in a transparent way, we consider ideal surfaces; that is, we disregard all complicating factors arising at real surfaces, as, for example, surface steps, impurities, anisotropies, or reconstruction. Given this scope, surface structures evolve through elementary atomic or molecular moves that obey fairly simple rules, but a sequence of a large number of moves eventually leads to a high degree of self-organization and to complex terminal structures on the nanoscopic or even mesoscopic scale.

Figure 1(a) illustrates some types of atomic moves, which dominate the early stages of growth. Following deposition to the substrate surface, atoms can reevaporate or stick to the surface and perform diffusional steps. Diffusing adatoms (monomers) can stick together when they meet, forming dimers, trimers, or larger two-dimensional islands. Islands as a whole in general do not diffuse; they grow by attachment of other adatoms or decay by dissociation. Three-dimensional growth is due to direct deposition on top of an island that has

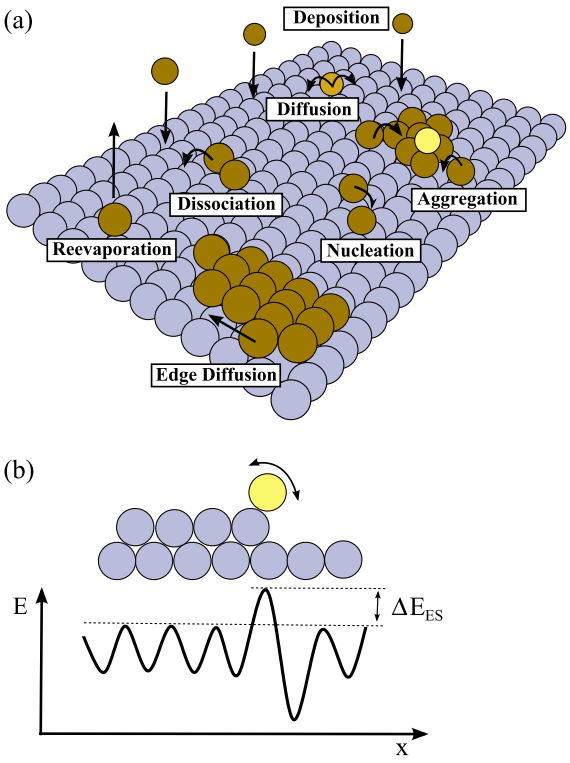

FIG. 1 (color online). Illustration of (a) elementary moves during growth after deposition onto a surface and (b) the Ehrlich-Schwoebel barrier for crossing the step edge.

formed before, or to interlayer jumps. In an interlayer jump, illustrated in Fig. 1(b), the atom in general must surmount an additional energy barrier, the so-called Ehrlich-Schwoebel barrier associated with a low-coordinated site at a step edge (Ehrlich and Hudda, 1966; Schwoebel, 1969).

Structure formation begins with the assembly of two-dimensional islands, composed of adsorbate atoms within the first monolayer. Usually a range of fairly low temperatures exists, where reevaporation can be ignored and thermal energies k_BT are significantly lower than the binding energy E_B between two adatoms, while diffusion is active. The condition $k_BT \ll E_B$ ensures that only a few atoms are required to form a stable island. An important concept is the critical island size (*critical nucleus*). Islands composed of more than i atoms are more likely to grow than to decay.

Two factors influence the nucleation and growth of islands: deposition of atoms onto the surface with a flux F and thermally activated diffusion of adatoms along the surface with a diffusion coefficient

$$D \simeq D_\infty \exp(-U/k_BT), \tag{1}$$

where U is the diffusion barrier. For atomic systems, the preexponential factor is given by $D_\infty = \nu a^2$, where ν is an attempt frequency and a is the lattice constant of the substrate. The mean time for a unit cell to be hit by an atom is $1/Fa^2$, and a^2/D is the mean time after which it leaves that cell by diffusion. Growth kinetics are controlled by the dimensionless ratio of these times, the D/F ratio $\Gamma = D/Fa^4$. In the following, a is used as a length unit and is not always given explicitly.

Because adatom diffusion is thermally activated, the density N of stable islands is a sensitive function of temperature. At high temperatures, D is large and adatoms can diffuse over longer distances before encountering another adatom or attaching to an island. Accordingly, N becomes smaller with increasing T. This is demonstrated in Fig. 2 for fullerene (C_{60}) islands grown on an atomically flat $CaF_2(111)$ surface (Loske *et al.*, 2010).

Rate equations (RE) have proven to be very useful to relate measured island densities to atomistic parameters (Zinsmeister, 1966; Venables, 1973). The approach follows

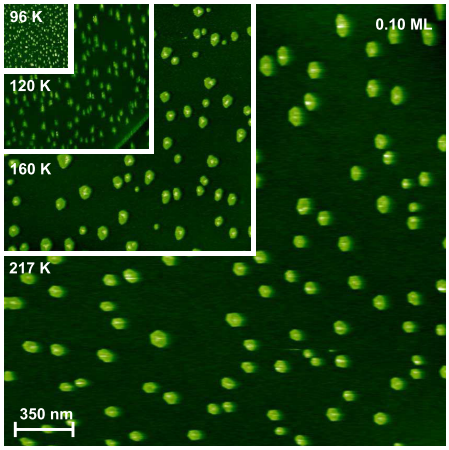

FIG. 2 (color online). AFM images of C_{60} molecules on $CaF_2(111)$ at a coverage $\Theta = 0.1$ for different substrate temperatures between 96 and 217 K. From Loske *et al.*, 2010.

the spirit of classical nucleation theory by Becker and Döring (1935) and is based on equations for the evolution of densities $n_s(t)$ of islands composed of s atoms. Monomers have a density $n_1(t) \equiv n(t)$. Islands with $s \geq 2$ are considered to be immobile. This leads to the infinite set of equations

$$\frac{dn}{dt} = F - 2D\sigma_1 n^2 - Dn\sum_{s=2}^{\infty}\sigma_s n_s + 2K_2 n_2 + \sum_{s=3}^{\infty} K_s n_s, \tag{2a}$$

$$\frac{dn_s}{dt} = D\sigma_{s-1} n n_{s-1} - D\sigma_s n n_s + K_{s+1} n_{s+1} - K_s n_s, \quad s = 2, 3, \ldots. \tag{2b}$$

Attachment of diffusing monomers to s clusters occurs with rates $\sigma_s D n n_s$, where σ_s are called capture numbers. Detachment of monomers from s clusters occurs with rates K_s, where $K_s = 0$ if $s > i$. Reevaporation of atoms, direct impingement of arriving atoms onto clusters, coalescence of clusters, or dissociation of clusters into subclusters are neglected in Eqs. (2) but can be incorporated by proper extension (Venables, Spiller, and Hanbücken, 1984; Brune, 1998; Venables, 2000).

A straightforward step in refining Eqs. (2) is to distinguish the impingement of atoms to the free surface from impingement to the islands edge or to the top of an island and subsequent attachment to its edge. F is then replaced by $F(1-\Theta)$ and terms of the form $F\kappa_s n_s$ are added, where κ_s is a direct capture area (Venables, 1973). In Sec. IV we refer to the corresponding rate equations as the refined RE.

From the above concepts it is clear that cluster growth on surfaces basically differs from growth in solutions. There small clusters composed of only a few atoms (molecules) are generally unstable due to solvation effects. This implies that the critical nuclei are large, in contrast to metallic surface growth. In standard continuum theory they are characterized by a critical radius, which results from the competition of the surface free energy, increasing as R^2, and the bulk free energy, proportional to R^3. Cluster diffusion and cluster aggregation that both are affected by hydrodynamic effects play an important role in distinction to processes shown in Fig. 1. Moreover, crystal growth in the solution involves many metastable intermediates. The large variety of intermediate structures generally has no analog in surface growth. Finally, the buildup of crystalline structures is associated with release of latent heat, which requires the introduction of a temperature field and heat diffusion equation into the theory.

III. HOW MANY ISLANDS FORM?

A. Island densities of one-component adsorbates

To predict from Eqs. (2) the dependence of density $N = \sum_{s=i+1} n_s$ of stable islands on Γ, it is sufficient to replace σ_s for $s > i$ by an averaged capture number $\bar{\sigma}$,

$$\bar{\sigma} = \frac{1}{N}\sum_{s=i+1}^{\infty}\sigma_s n_s. \tag{3}$$

In addition, a quasistationary state for unstable islands of size $2 \leq s \leq i$ is assumed, where decay and aggregation processes nearly balance each other, $K_s n_s \simeq D\sigma_{s-1} n n_{s-1}$,

yielding $n_s \propto n^s$. Since a monomer, when it gets detached from an s cluster, has to overcome an energy barrier that is composed of both its binding energy $(E_{s-1} - E_s)$ to the cluster and the diffusion barrier, one can write $K_s = \mu_s D \exp[-(E_s - E_{s-1})/k_B T]$, where μ_s is a constant. Here $E_s > 0$ is the total energy needed to decompose an s cluster into monomers ($E_1 = 0$). In this way one arrives at the so-called Walton relations (Walton, 1962)

$$n_s \simeq b_s \exp(E_s/k_B T) n^s, \qquad s = 2, \ldots, i, \tag{4}$$

where $b_s = \prod_{j=1}^{s-1} \sigma_j/\mu_{j+1}$.

Summation of Eq. (2b) over $s > i$ leads to a cancellation of all terms on the right-hand side except the term $s = i$. Using Eqs. (3) and (4) the rate equations (2) reduce to a closed set of equations for $n(t)$ and $N(t)$,

$$\frac{dn}{dt} = F - (1 + \delta_{i,1})\sigma_i D n n_i - \bar{\sigma} D n N, \tag{5a}$$

$$\frac{dN}{dt} = \sigma_i D n n_i, \tag{5b}$$

with $n_i \propto n^i$ from Eq. (4). The last equation simply tells that $N(t)$ grows by nucleation events.

Experimental Γ values are very large compared to unity, typically $10^5 < \Gamma < 10^{11}$. Values of that order are often representative of the leading asymptotic behavior in the limit $\Gamma \to \infty$. An asymptotic solution of Eqs. (5) in this limit can be derived from the scaling ansatz $n(\Gamma, \Theta) \sim \Gamma^{-\zeta} n_\infty(\Theta)$ and $N(\Gamma, \Theta) \sim \Gamma^{-\chi} N_\infty(\Theta)$ with $\zeta, \chi > 0$ (Dieterich, Einax, and Maass, 2008). Note that both n and N should decrease with increasing Γ at fixed Θ. Inserting this scaling ansatz into Eqs. (5) gives $\zeta = 2/(i + 2)$ and $\chi = i/(i + 2)$. Finally,

$$N(\Gamma, \Theta) \sim \left[\frac{(i + 2)\sigma_i b_i}{\bar{\sigma}^{i+1}} \Theta\right]^{1/(i+2)} e^{E_i/(i+2)k_B T} \Gamma^{-i/(i+2)}, \tag{6a}$$

$$n(\Gamma, \Theta) \sim \frac{1}{\bar{\sigma} \Gamma N(\Gamma, \Theta)}. \tag{6b}$$

Equation (6b) is often used in the literature as a "quasistationary" approximation in Eqs. (5) to derive Eq. (6a). Our derivation is more general and shows that this quasistationary relation becomes exact in the $\Gamma \to \infty$ limit. Its range of validity for finite Γ can be estimated from the first-order corrections $\Delta N(\Gamma, \Theta)$ and $\Delta n(\Gamma, \Theta)$ to the solution (6). In the case $i = 1$, for example, both ratios $\Delta N(\Gamma, \Theta)/N(\Gamma, \Theta)$ and $\Delta n(\Gamma, \Theta)/n(\Gamma, \Theta)$ are found to behave as $\sim(\Theta^2\Gamma)^{-1/3}$, and the criterion for Eq. (6a) to hold is

$$(\Theta^2\Gamma)^{1/3} \gg \left(\frac{64\sigma_1}{9\bar{\sigma}^2}\right)^{1/3}, \tag{7}$$

where the right-hand side is of order unity. The smaller Θ is, the larger Γ is in order for the scaling solutions (6) to remain valid. For $i = 1$ the ratio $N(\Gamma, \Theta)/n(\Gamma, \Theta)$ also behaves as $\sim(\Theta^2\Gamma)^{1/3}$ according to Eqs. (6). This means that the applicability of Eqs. (6) is equivalent to the experimentally testable condition $n(\Gamma, \Theta) \ll N(\Gamma, \Theta)$. Because Γ is large, this condition is well satisfied in a large range of Θ before N steeply falls in the coalescence regime, which typically sets in near $\Theta \approx 0.2$. In other words, the scaling of the island density with respect to Γ is not restricted to a "saturation regime" of nearly Θ-independent island density, although this regime preceding island coalescence is certainly most convenient for experiments. An alternative argument for obtaining the crossover to the stationary regime was given earlier by equating Eq. (6a) with the solution for N in the initial time regime (Evans, Thiel, and Bartelt, 2006).

Measurements of N as a function of F and T allow one to extract critical island sizes, diffusion coefficients, and binding energies. Via the Γ-dependent factor in Eq. (6a) one first determines i. In practice, because T competes with the binding energy E_B, i is constant only within certain temperature intervals and overall increases with T. This is illustrated in Fig. 3 for the system Ag/Pt(111) (Brune, 1998). Knowing i, the slopes in an Arrhenius representation of N yield $(iU + E_i)/(i + 2)$ as the activation energy, which for $i = 1$ is $U/3$. The high-T extrapolation of N in addition allows one to obtain information about the preexponential factor D_∞. This "nucleation route" (Brune *et al.*, 1994; Müller *et al.*, 1996; Brune, 1998; Barth *et al.*, 2000) to measuring surface diffusion coefficients and binding energies has been found particularly useful. Examples are diffusion of Pd diffusion on $SrTiO_3(100)$ (Richter and Wagner, 2005), of Co diffusion on Cu(111) (Prieto, de la Figuera, and Miranda, 2000), or of C_{60} molecules on $CaF_2(111)$ (Loske *et al.*, 2010), and of hydrogenated tetraphenyl porphyrin (2H-PPT) on Ag (111) (Rojas *et al.*, 2011). A thorough overview on similar analyses of surface diffusion on metals can be found in Antczak and Ehrlich (2010).

For a quantitative description of N beyond Γ scaling, it turns out that the approximation (3) of constant capture numbers is insufficient. In particular, the Θ dependence predicted by Eq. (6a) does not account for the tendency for N to saturate at large Θ before the coalescence regime. A good quantitative account is provided by a self-consistent theory of the capture numbers, which will be discussed in Sec. III.C.

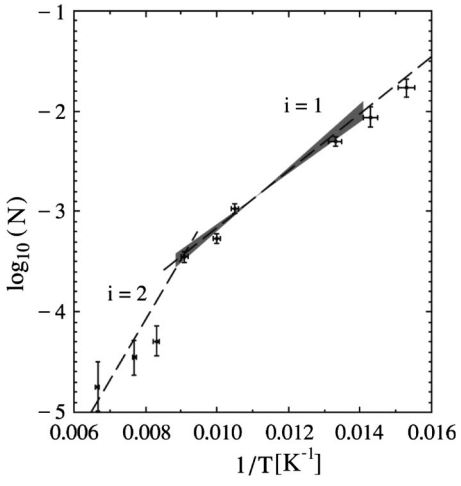

FIG. 3. Island densities of Ag on Pt(111) at coverages $\Theta = 0.12$ in an Arrhenius plot. Analysis of the slope with Eq. (6a) in the low-temperature regime, where $i = 1$, gives a diffusion barrier $U = 0.168 \pm 0.005$ eV. In the high-temperature regime, where $i = 2$, the slope yields a dimer bonding energy $E_2 = 0.15 \pm 0.02$ eV. From Brune *et al.*, 1999.

The rate equations form a very useful basis for treating problems in more complicated situations. Extensions of the theory for predicting island densities of multicomponent adsorbates are discussed in Secs. III.B and III.C. A beautiful example is the growth of graphene on metallic surfaces, induced by deposition of carbon atoms or hydrocarbon molecules. Nucleation can then proceed via a two-step process. Clusters of five carbon atoms, which still are mobile, form first. In turn, six such clusters react to a stable, immobile graphene island (Zangwill and Vvedensky, 2011). Measured carbon adatom densities on Ru(0001) (Loginova *et al.*, 2008) could be analyzed in terms of coupled rate equations for the densities of adatoms (n), five-atom clusters (c), and stable islands (N), thereby giving insight into the detailed kinetics of this more complicated nucleation scenario. Because of the large "critical nuclei" in this case, one has $n \gg c \gg N$. Note that due to the scaling $n/N \sim \Gamma^{(i-2)/(i+2)}$, cf. Eq. (6), $n \gg N$ is in general expected to hold for $i > 2$.

Epitaxial growth of graphene was indeed observed on several metallic surfaces (Castro Neto *et al.*, 2009; Voloshina and Dedkov, 2012) such as Ru(0001) (Loginova *et al.*, 2008; Zhou, Gao, and Goodman, 2010), Ir(111) (Coraux *et al.*, 2009; Rusponi *et al.*, 2010), Pt(111) (Sutter, Sadowski, and Sutter, 2009; Gao *et al.*, 2011), Ni(111) (Grüneis and Vyalikh, 2008), and Cu(111) (Gao, Guest, and Guisinger, 2010). Single-layer graphene on metal surfaces as well as chemically modified graphene and few-layer graphene can conversely be used as a substrate for the growth of metals such as Ag, Au, Fe, Pt, and Ti. Such substrates modify the energetics of adsorbed metal atoms, allowing the production of a variety of metallic nanoparticle structures [for details, see Pandey *et al.* (2011) and Moldovan *et al.* (2012)].

B. Island densities of binary alloys

For binary (or multicomponent) alloys, growth kinetics are controlled by an enlarged set of parameters including mixing ratios and surface diffusion coefficients, which can vary strongly among different atomic species. This poses the question of a multiparameter scaling of island densities. Moreover, atoms of different types will differ in their mutual binding energies on the surface, which can lead to a competition of different nucleation paths. The coexistence of critical nuclei with different compositions together with asymmetries in adatom diffusion coefficients leads to new crossover phenomena in the scaling of island densities. Detection of such crossovers by experiment and interpretation with the help of theoretical predictions, described below, should allow one to deduce novel information on the size and composition of critical nuclei, in particular, on the binding energies of unlike atoms in the presence of the surface.

Consider two species of atoms $\alpha = A$ and B to be codeposited with partial fluxes $F_\alpha = x_\alpha F$, where $F = F_A + F_B$ is the total flux. In this way a binary alloy with mole fractions x_A and $x_B = 1 - x_A$ is formed. Only monomers of densities n_α are supposed to diffuse along the surface with diffusion coefficients $D_\alpha = \nu_\alpha \exp(-U_\alpha/k_BT)$, while clusters with more than one atom ($s > 1$) are immobile.

To elucidate the essential new physics compared to one-component systems, we limit our discussion to cases where the largest unstable clusters are composed of not more than two atoms [for the general treatment, see Einax, Ziehm *et al.* (2007)]. Stable islands of density N, in particular, trimers and larger clusters, are treated in an averaged manner irrespective of composition. Monomers with densities n_α and all combinations of dimers (densities $n_{\alpha\beta}$) will be treated explicitly. Considering systems where the important differences between A and B atoms primarily arise from diffusion coefficients and fluxes, we do not distinguish between A and B atoms in their respective capture numbers.

In comparison with Eq. (2a) the equation of motion for A monomers involves additional terms due to the capture of B atoms and to the decay of AB dimers. Similarly the rate equations for the dimer density involve additional terms. The structure of these equations is quite obvious. For example, for $n_{AB}(t)$ the rate equation is

$$\frac{dn_{AB}}{dt} = (D_A + D_B)\sigma_1 n_A n_B - \Big(\sum_\beta D_\beta n_\beta\Big)\sigma_2 n_{AB} - K_{AB} n_{AB}. \tag{8}$$

Note that the coefficient for relative diffusional motion of A and B monomers is $D_A + D_B$. $K_{\alpha\beta} = K_{\beta\alpha}$ denote the dissociation rates of dimers. A reduced set of rate equations for $n_\alpha(t)$, $n_{\alpha\beta}(t)$, and $N(t)$ is thus obtained, which allows us to derive the scaling behavior of island densities.

In experiments with binary systems both conditions $\Gamma_\alpha = D_\alpha/F \gg 1$ hold in general and a scaling analysis similar to that for monocomponent adsorbates can be worked out. The simplest situation arises when all dimers are stable. This corresponds to the case $i = 1$, where

$$N \simeq \left(\frac{3\sigma_1\Theta}{\bar{\sigma}^2}\right)^{1/3} \Gamma_{\rm eff}^{-1/3}. \tag{9}$$

The exponents agree with those in Eq. (6a) for one-component systems, but the scaling variable $\Gamma_{\rm eff} = D_{\rm eff}/F$ with $D_{\rm eff} = D_A D_B/(x_A D_B + x_B D_A)$ now describes the influence of both the different diffusion coefficients and mole fractions of the two species. Clearly, the species with the lower diffusion coefficient governs the dependence of N on temperature.

If all dimers are unstable ($i = 2$), we first have to seek for generalized Walton relations (Einax, Ziehm *et al.*, 2007) to express dimer densities in terms of adatom densities. As in Sec. III.A, these are obtained by nearly balancing the formation and dissociation of dimers,

$$\sigma_1 D_\alpha n_\alpha^2 \simeq K_{\alpha\alpha} n_{\alpha\alpha}, \qquad \alpha = A, B, \tag{10}$$

$$\sigma_1 (D_A + D_B) n_A n_B \simeq K_{AB} n_{AB}. \tag{11}$$

Writing $K_{\alpha\beta} = \mu_{\alpha\beta} D_{\alpha\beta} \exp(-E_{\alpha\beta}/k_{\rm B}T)$ in terms of the diffusion coefficients $D_{\alpha\alpha} = D_\alpha$, $D_{AB} = (D_A + D_B)/2$, and the dimer binding energies $E_{\alpha\beta} \geq 0$ (with $\mu_{\alpha\beta}$ being constants), one obtains

$$N \simeq \left(\frac{4\sigma_1\sigma_2\Theta}{\bar{\sigma}^3}\right)^{1/4} \left[\sum_{\alpha,\beta} \mu_{\alpha\beta}^{-1} e^{E_{\alpha\beta}/k_BT} \frac{F_\alpha F_\beta}{D_\alpha D_\beta}\right]^{1/4}. \tag{12}$$

Equations (9) and (12) generalize the scaling relation (6a) for $i = 1, 2$ to the binary case. The predictions are in excellent

agreement with KMC simulations (Einax, Ziehm *et al.*, 2007), but still await experimental confirmation. Because of the dependence of N on E_{AB} in Eq. (12), binding energies between *unlike* atoms on a substrate should become accessible by experiment. To achieve this, U_α and $E_{\alpha\alpha}$ can first be determined under deposition of only one species and then N is measured under codeposition. The feasibility of a corresponding procedure has been demonstrated by recovering all growth parameters from a "computer experiment" on island densities, in a way equivalent to analyzing a true experiment [for details, including consistency checks, see Einax, Dieterich, and Maass (2009)].

More complex situations arise when dimers with different compositions have different stability. For example, only BB dimers could be unstable ($K_{AA} = K_{AB} = 0, K_{BB} > 0$), or only AA dimers could be stable (K_{AB}, $K_{BB} > 0$, $K_{AA} = 0$). For these and similar situations a closed rate equation for N can be derived by factorizing dimer densities in terms of the adatom densities with the help of Eqs. (10) and (11), and by expressing the adatom densities through N via the quasistationary condition analogous to Eq. (6b). In all cases this leads to

$$\frac{dN}{d\Theta} = \frac{b}{N^2} + \frac{c}{N^3}. \tag{13}$$

The linear combination on the right-hand side reflects nucleation via the dimer ($dN/d\Theta \sim N^{-2}$) and trimer routes ($dN/d\Theta \sim N^{-3}$).

The full solution of Eq. (13) is given by

$$N = (c/b)\psi(b^4\Theta/c^3), \tag{14}$$

where $\psi(\cdot)$ is determined by a transcendental equation (Einax, Ziehm *et al.*, 2007). The coefficients b and c in Eq. (13) depend on Γ_α and x_α, and their detailed form is given in Dieterich, Einax, and Maass (2008). If, for example, stable dimers are of AA type only, then $b \propto F_A/D_A$, and c is a sum of two terms proportional to F_AF_B/D_AD_B and to $(F_B/D_B)^2$, corresponding to the two paths of trimer formation via AB and BB dimers. Each possible nucleation path in the above examples contributes additively to $dN/d\Theta$. The dimer route is dominating for fast B diffusion and x_A large, and the trimer route for slow B diffusion and x_B large. The smooth crossover is validated in Fig. 4, where KMC data for N versus D_B/F are plotted for a situation with stable AA dimers ($K_{AA} = 0$) and zero binding energies of AB and BB dimers.

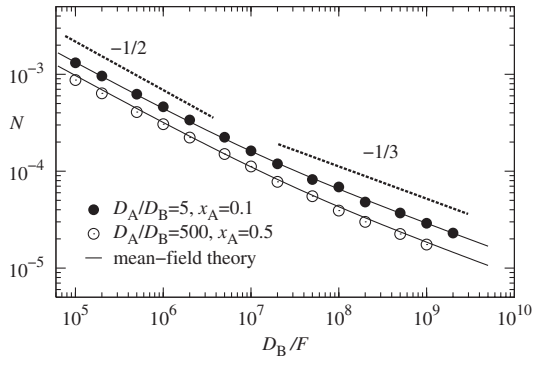

FIG. 4. Simulated number densities N of stable islands at coverage $\Theta = 0.1$ as a function of D_B/F, when AA dimers are stable, while AB and BB dimers are unstable. The solid lines correspond to the full solution (14) and the dashed lines indicate the change of scaling behavior associated with the dimer and trimer nucleation routes. From Einax, Ziehm *et al.*, 2007.

C. Beyond Γ scaling: Self-consistent capture numbers

The efficiency of islands to capture monomers is affected by the shielding by other islands in their neighborhood. Such shielding effects can be treated approximately by capture numbers that depend on the whole set of monomer and island densities (Bales and Chrzan, 1994; Bales and Zangwill, 1997). The idea is to consider the diffusion equation for the local adatom profile $\tilde{n}(r, t)$ around an s cluster with radius $R_s = (s/\pi)^{1/2}$ in the presence of the flux F and an effective medium with absorption rate D/ξ^2,

$$\left(\frac{\partial}{\partial t} - D\Delta\right)\tilde{n}(r, t) = F - \frac{D}{\xi^2}\tilde{n}(r, t), \tag{15}$$

where D/ξ^2 is identified with the loss terms in Eq. (2a),

$$\xi^{-2} = 2\sigma_1 n + \sum_{s\geq 2}\sigma_s n_s. \tag{16}$$

The sum over s can be replaced by $\bar{\sigma}N$ as before, leading to a reduced self-consistent description already considered by Venables (1973). In a quasistationary state, $\partial_t\tilde{n} \simeq 0$, $D\xi^{-2}n \simeq F$, and Eq. (15) becomes

$$\Delta\tilde{n}(r) - \frac{1}{\xi^2}[\tilde{n}(r) - n] = 0. \tag{17}$$

For large r, $\tilde{n}(r)$ should approach its mean value n considered in the rate equations and at the island edge $r = R_s$, it must be zero in the absence of detachment processes [case $i = 1$; for a generalization to higher i, see Bales and Zangwill (1997)]. With these boundary conditions, the solution of Eq. (17) becomes $\tilde{n}(r) = n[1 - K_0(r/\xi)/K_0(R_s/\xi)]$, where $K_\nu(\cdot)$ denotes the modified Bessel function of order ν. Equating the inward current of adatoms $2\pi R_s D(\partial\tilde{n}/\partial r)_{r=R_s}$ at the island edge with the aggregation rate $\sigma_s Dn$, one obtains

$$\sigma_s = \frac{2\pi R_s}{n}\left(\frac{\partial\tilde{n}}{\partial r}\right)_{r=R_s} = 2\pi\frac{R_s}{\xi}\frac{K_1(R_s/\xi)}{K_0(R_s/\xi)}. \tag{18}$$

The merit of this approach is that a good quantitative description of n and N as a function of Θ is provided despite the fact that σ_s themselves are not well predicted, as discussed later [cf. Fig. 6(a)].

For a generalization of the self-consistent theory to multicomponent systems, many-particle densities need to be introduced to obtain expressions for capture numbers that are symmetric under the exchange of atomic species (Einax, Maass, and Dieterich, 2013). The method is best illustrated by considering the reaction rate $(D_A + D_B)\sigma_1^{AB}n_An_B$ of A and B monomers to form AB dimers in the case of binary alloys with $i = 1$. The effective medium in this case is characterized by two mean free paths ξ_α, $\alpha = A, B$, which result from the loss terms $(D_\alpha/\xi_\alpha^2)n_\alpha$ in the rate equations of the monomer densities. Considering the pair distribution function of A and B monomers, this function satisfies a diffusion equation with symmetric diffusion coefficient $D_A + D_B$ and symmetric absorption rate $\sum_\alpha D_\alpha\xi_\alpha^{-2}$. Taking into account the boundary

conditions, the final result for σ_1^{AB} has the same structure as in the one-component theory (Bales and Chrzan, 1994),

$$\sigma_1^{AB} = 2\pi \frac{R_1}{\xi_{\rm eff}} \frac{K_1(R_1/\xi_{\rm eff})}{K_0(R_1/\xi_{\rm eff})} \tag{19}$$

with an effective mean free path $\xi_{\rm eff}$. In contrast to the one-component theory this mean free path depends on the diffusion coefficients,

$$\xi_{\rm eff}^{-2} = (D_A + D_B)^{-1}[D_A \xi_A^{-2} + D_B \xi_B^{-2}]. \tag{20}$$

One can show that $\sigma_1^{\alpha\alpha}$ is also given by Eq. (19) with $\xi_{\rm eff}$ replaced by ξ_α. To get σ_s^α for $s > 1$ one has in addition to replace R_1 by R_s.

As in the monocomponent case, an extension is possible also to include decay processes of clusters. The capture and decay rates in this extension are consistent with the generalized (two-component) Walton relations. Again a good quantitative description of island densities is obtained. As an example we show in Fig. 5 the calculated number densities N, n_α, and $n_{\alpha\alpha}$ for mixed dimer stabilities in comparison with KMC data.

For critically testing the theory outlined here, it is important to provide experimental data for island densities in multicomponent systems. A particular challenge is to simultaneously measure the densities of the individual monomers or, more generally, the densities of the subcritical clusters. This is already highly desirable for monocomponent systems, because it allows one to test basic assumptions of the rate equation approach. For example, to our knowledge, neither the Walton relation (4) nor their generalized forms (10) and (11) have been tested in experiments.

To sum up, using rate equations and KMC simulations, it was shown that even for binary systems comparatively simple (multiparameter) scaling relations can be established that describe the densities of stable islands as a function of adatom diffusion coefficients and partial deposition fluxes. Equation (18) entails a generalization to binary systems of the well-known nucleation route for obtaining microscopic parameters from island density measurements. In practice, this equation

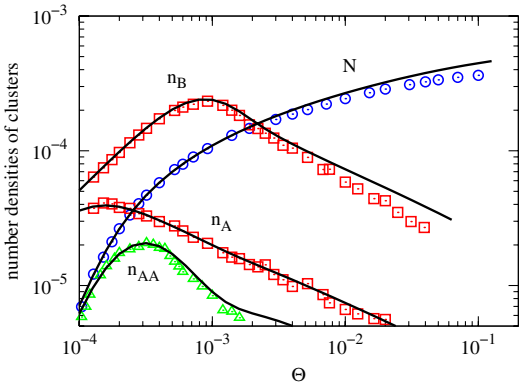

FIG. 5 (color online). Number densities of A and B adatoms, AA dimers, and stable islands as a function of the coverage Θ for a case of mixed dimer stabilities, where AA dimers are stable, while AB and BB dimers are unstable with zero binding energies. Results from the self-consistent approach (solid lines) are compared with KMC simulations (symbols). Parameters are $x_A = x_B = 1/2$, $D_A/F = 10^8$, and $D_B/F = 10^7$.

can be utilized to determine binding energies between unlike atoms in the presence of the surface. It would be interesting to compare these results with corresponding ones from electronic structure calculations. A particularly interesting feature is the occurrence of novel crossover phenomena in the island densities, which emerge when critical nuclei of different composition compete with each other in determining the dominant nucleation pathway. A detailed quantitative description of island densities is possible, when considering many-particle densities in self-consistent theories for capture numbers. Also decay processes of unstable clusters can be treated successfully within this framework.

IV. WHAT IS THE DISTRIBUTION OF ISLAND SIZES?

A. Predictions from rate equations

More detailed information of the submonolayer growth kinetics is contained in the island size distribution (ISD) $n_s(\Theta, \Gamma)$. Imagine that the capture numbers σ_s in Eqs. (2) were known. Can we then expect that the RE predict the ISD in the precoalescence regime? This would mean that many-particle correlation effects can be incorporated in effective capture numbers, and that spatial fluctuations in shapes and capture zones of islands as well as coalescence events, despite rare in the early-stage growth, are negligible.

While Eq. (18) already implies that capture numbers have to be regarded as effective ones, $\sigma_s = \sigma_s(\Theta, \Gamma)$, their full dependence on both island size s and external parameters has been determined recently in an extensive KMC study of models yielding different island morphologies (Körner, Einax, and Maass, 2010, 2012). In Fig. 6(a) we show representative results of this study for kinetic growth with hit-and-stick aggregation on a (100) surface. Integrating the refined RE [see discussion after Eqs. (2)] under consideration of the full Θ dependence of $\sigma_s(\Theta, \Gamma)$ indeed gives a good description of the ISD, as demonstrated in Fig. 6(b). To achieve this good agreement it is necessary to take into account details in the functional form of $\sigma_s(\Theta, \Gamma)$. For example, when neglecting the Θ dependence by setting $\sigma_s(\Theta, \Gamma) = \sigma_s(\Theta_0, \Gamma)$ for a fixed reference coverage Θ_0, a good description is not obtained. It is moreover important to point out that for compact island morphologies the good agreement is of limited practical use, because coalescence events, not considered in the RE, become relevant already at rather small coverages of about 5%.

Since the refined RE with those simulated Θ-dependent σ_s were shown to be suitable for predicting the ISD, the challenge is to find an accurate description of the functional form of the $\sigma_s(\Theta, \Gamma)$. Unfortunately $\sigma_s(\Theta, \Gamma)$ shows a high sensitivity with respect to the island morphologies and probably also to details of the growth kinetics. A general feature is that for island sizes s larger than the mean island size $\bar{s}$, $\sigma_s(\Theta, \Gamma)$ increases linearly with s, $\sigma_s(\Theta, \Gamma) \sim c_1(\Theta, \Gamma) + c_2(\Theta, \Gamma)s$. This can be reasoned by considering the areas for adatom capture surrounding the islands (Evans, Thiel, and Bartelt, 2006). However, even for this generic feature the functions $c_j(\Theta, \Gamma)$ depend on details of the attachment kinetics (hit and stick or with limited edge diffusion, etc.). For improving theories for the ISD, it was argued that correlation effects

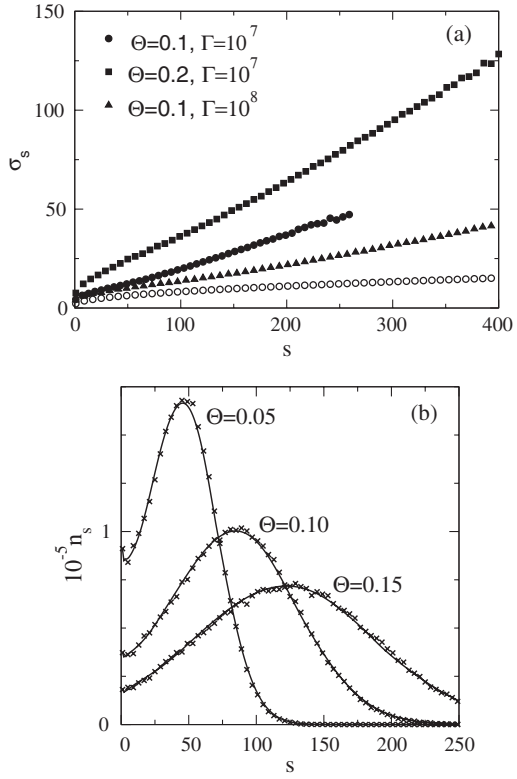

FIG. 6. (a) Capture numbers and (b) island size distributions from KMC simulations of kinetic growth with hit-and-stick aggregation on a (100) surface. In (a) the open circles refer to the prediction of the self-consistent theory for $\Theta = 0.1$ and $\Gamma = 10^7$, which for large s deviate strongly from the true $\sigma_s(\Theta, \Gamma)$ (full circles). In (b) the solid lines are the solution of the rate equation (2) with the simulated $\sigma_s(\Theta, \Gamma)$ as input. From Körner, Einax, and Maass, 2012.

between island sizes and capture areas need to be taken into account. This can be achieved by considering the joint probability of island size and capture area (Mulheran and Robbie, 2000; Amar, Popescu, and Family, 2001; Popescu, Amar, and Family, 2001; Evans and Bartelt, 2002; Mulheran, 2004).

B. Scaling approaches

While a theoretical description of the details in $\sigma_s(\Theta, \Gamma)$ seems to be out of reach, a simpler approach to the ISD becomes possible when assuming that the dependence of $n_s(\Theta, \Gamma)$ on Θ and Γ is mediated by the mean island size $\bar{s}(\Theta, \Gamma)$. In this case the ISD should obey the following scaling form, as first suggested by Vicsek and Family (1984):

$$n_s(\Theta, \Gamma) = \frac{\Theta}{\bar{s}^2(\Theta, \Gamma)} f\left(\frac{s}{\bar{s}(\Theta, \Gamma)}\right). \tag{21}$$

Here the scaling function $f(x)$ must fulfill the normalization and first moment conditions $\int_0^\infty f(x)dx = \int_0^\infty xf(x)dx = 1$, because $\sum_s n_s \simeq N \simeq \Theta/\bar{s}$ and $\sum_s s n_s = \Theta$.

An explicit expression for $f(x)$ with a shape independent of Θ was suggested by Amar and Family (1995),

$$f(x) = C_i x^i \exp(-i a_i x^{1/a_i}), \tag{22}$$

where the parameters C_i and a_i follow from the above conditions on f. Equation (22) was believed to be independent even of the morphology (Amar and Family, 1995), but this was later questioned (Bartelt and Evans, 1996; Evans, Thiel, and Bartelt, 2006). The dependence of Eq. (22) on i allows one to determine the size of the critical nucleus from measurements of the ISD (Ruiz *et al.*, 2003; Pomeroy and Brock, 2006; Loske *et al.*, 2010; Potocar *et al.*, 2011).

It is interesting to note that a semiempirical form, which has a structure similar to Eq. (22), was suggested by Pimpinelli and Einstein (2007) for the distribution of capture-zone areas A as identified by Voronoi tessellation,

$$P_\beta = c_\beta a^\beta \exp(-d_\beta a^2), \tag{23}$$

where $a = A/\bar{A}$ is the capture zone rescaled with respect to the mean $\bar{A}$ and $\beta = i + 2$ (Li, Han, and Evans, 2010; Pimpinelli and Einstein, 2010).[1] The parameters c_β and d_β are again determined by normalization and a condition on the first moment.

This new theoretical result can alternatively be used to determine i. In fact, the capture-zone scaling was recently applied to determine critical island sizes in organic thin-film growth (Lorbek, Hlawacek, and Teichert, 2011; Potocar *et al.*, 2011; Tumbek *et al.*, 2012). For para-hexaphenyl (6P) molecules deposited on a sputter-modified muscovite mica (001) substrate, Potocar *et al.* (2011) reported that the combined analysis of the ISD according to Eq. (22) and the capture-zone distribution (23) gave convincing evidence for $i = 3$. More experiments in this direction should be performed to test the general validity of Eq. (23). In particular, the analysis should be extended to identify correlations between island size and capture-zone area. As mentioned (see Sec. IV.A), corresponding information is highly relevant to check theoretical considerations on the size dependence of capture numbers.

C. Limiting behavior for $D/F \to \infty$

Because the refined RE with the appropriate $\sigma_s(\Theta, \Gamma)$ predicts the ISD, it should be possible to derive an evolution equation for the scaled island density $f(x, \Theta, \Gamma) \equiv \bar{s}^2 n_{x\bar{s}}/\Theta$. Because of the normalization this function will approach a limiting curve $f_\infty(x, \Theta)$ for $\Gamma \to \infty$, and an interesting question is whether this curve is independent of Θ. To discuss this, we concentrate on the case $i = 1$. For large Γ, $\bar{s} \sim N^{-1} \sim \Gamma^{1/3}$, and $x = s/\bar{s}$ becomes a continuous variable. This allows one to consider a continuum version of the refined RE (Bartelt and Evans, 1996; Evans and Bartelt, 2001; Körner, Einax, and Maass, 2012), which gives a partial differential equation for $f(x; \Theta, \Gamma)$ in the variables x and Θ. This equation includes the scaled capture numbers $C(x, \Theta, \Gamma) = \sigma_{x\bar{s}}/\bar{\sigma}$ and scaled areas for direct capture $K(x, \Theta, \Gamma) = \kappa_{x\bar{s}}/\bar{\kappa}$. Taking the $\Gamma \to \infty$ limit then yields a determining equation for $f_\infty(x, \Theta)$. If f_∞ is independent of Θ, this equation becomes an ordinary differential equation that can be solved exactly (Bartelt and

[1] In the original work (Pimpinelli and Einstein, 2007) $\beta = i + 1$ was suggested [see also Oliveira and Aarão Reis (2011, 2012)].

Evans, 1996) and yields a power-law decay for large x. However, arguments presented by Oliveira and Aarão Reis (2012) support a stretched exponential decay of the scaling function.

To study this question of a Θ dependence of $f_\infty(x, \Theta)$ for different island morphologies in the case $i = 1$, one can use the simulated capture numbers $\sigma_s(\Theta)$, discussed in Sec. IV.A (Körner, Einax, and Maass, 2012). In addition, the connection of $f_\infty(x, \Theta)$ to the scaled capture numbers and areas in the limit $\Gamma \to \infty$ was studied. For the point island model (Bartelt and Evans, 1992), where islands have no extension and $\Theta = Ft$ plays the role of the deposition time, f_∞ indeed turned out to be independent of Θ, while for extended islands the results indicate that f_∞ exhibits a (weak) Θ dependence.

To conclude taking into account the full dependence of capture numbers on island size, coverage, and D/F ratio, the rate equation approach predicts well the ISD in the precoalescence regime. Moreover, analysis of ISDs and capture cone area distributions allow for a determination of i, independent of the methods presented in Sec. III. Further theoretical work is required in order to establish the behavior of the limiting curve $f_\infty(x)$.

V. WHEN DO ISLANDS SURVIVE UPON CONTINUED DEPOSITION?

With ongoing deposition, when multilayer growth sets in, two contrasting growth modes can arise. Islands in the first layer either grow in the lateral direction and coalesce before a new layer nucleates or stable nuclei form on top of them before coalescence. Which of these two cases is realized depends on the characteristic island radius R_c at the onset of second-layer nucleation: If R_c is larger than the mean distance $N^{-1/2}$ between islands, coalescence sets in before second-layer nucleation and a smooth layer-by-layer growth behavior is obtained. On the other hand, if R_c is smaller than $N^{-1/2}$, islands grow in the normal direction before a smooth layer has developed and the film topography becomes rough.

It is important to note that the occurrence of smooth or rough films is answered differently from a thermodynamic viewpoint, where it is dictated by surface tensions and associated wetting properties. In this context a rough Volmer-Weber, a smooth Van der Merwe, and an intermediate Stranski-Krastanov growth mode are distinguished (Pimpinelli and Villain, 1998). During growth, however, films are usually not in thermal equilibrium and the film topography is determined by kinetics rather than thermodynamics. Under nonequilibrium growth conditions, R_c is the decisive quantity that determines the film topography (Tersoff, Denier van der Gon, and Tromp, 1994; Rottler and Maass, 1999).

An important quantity controlling the size of R_c is the Ehrlich-Schwoebel or additional step edge barrier ΔE_{ES} that an atom has to surmount when passing an island edge. If ΔE_{ES} is large, the associated Boltzmann factor

$$W = \exp(-\Delta E_{\mathrm{ES}}/k_{\mathrm{B}}T) \tag{24}$$

becomes small and atoms can remain longer on top of islands, implying that second-layer nucleation becomes more likely.[2]

A. Second-layer nucleation rate

In order to develop a theory, which predicts how R_c depends on W and Γ, a precise definition of R_c is needed. More generally, consider at time t the fraction $f(t)$ of islands covered by stable clusters. This fraction is zero for small t and increases to 1 in some time window, after which all islands are covered. At a time t_c half of the islands are covered, $f(t_c) = 0.5$, and the critical radius R_c can be conveniently defined by $R_c = R(t_c)$, where $R(t)$ denotes the mean island radius at time t. We define by $\Omega(R)$ the second-layer nucleation rate. The fraction of covered islands then is (Tersoff, Denier van der Gon, and Tromp, 1994)

$$f(t) = 1 - \exp\left(-\int_0^t dt' \Omega(R(t'))\right), \tag{25}$$

and the problem reduces to determine $\Omega(R)$ in dependence of W and Γ.

The functional form of $\Omega(R)$ can be deduced from scaling arguments (Rottler and Maass, 1999; Heinrichs, Rottler, and Maass, 2000; Krug, 2000; Krug, Politi, and Michely, 2000). To this end we consider a state where in total n adatoms are simultaneously on top of an island of size R. A number of $i + 1$ adatoms encounter at a point of the island with a probability $\sim(a^2/\pi R^2)^{(i+1)} \prod_{k=0}^{i}(n-k)$, where the product takes into account that there are $n(n-1)/2$ possibilities to form an (intermediate) pair, and, for $i > 1$, $(n-2) \times (n-3) \cdots \times (n-i)$ further possibilities for the remaining $i-1$ adatoms to attach to the pair. Multiplying this probability with the adatom diffusion rate D/a^2 and integrating over the island area (factor πR^2) yields the encounter rate of $i + 1$ atoms in the presence of $n \geq i + 1$ atoms on an island of size R[3]:

$$\omega_n(R) = \kappa_e \frac{D}{a^2}\left[\prod_{k=0}^{i}(n-k)\right]\left(\frac{a^2}{\pi R^2}\right)^i. \tag{26}$$

Logarithmic corrections need to be included in Eq. (26) when taking into account the fact that the encounter problem involves the number of distinct sites visited by a diffusing adatom (Politi and Castellano, 2003).

The decay time $\tau_n(R)$ of a state with n noninteracting adatoms on top of an island is the nth fraction of the lifetime $\tau_1(R)$ of one adatom. The latter is given by the typical time $\sim R^2/D$ to reach the island edge plus the time $\sim Ra/D$ to return to the edge, which on average takes place W^{-1} times

[2]The step edge barrier can be an effective one, i.e., $\Delta E_{\mathrm{ES}} = -k_{\mathrm{B}}T \ln\langle\exp(-\Delta E_\alpha/k_{\mathrm{B}}T)\rangle$, where $\langle\cdots\rangle$ denotes an average over microscopic step edge barriers ΔE_α for different local atomic configuration α at the island edge. Moreover, a factor ν_s/ν_{isl} needs to be included in Eq. (24) if the attempt frequency ν_s for hops down the step edge is different from the attempt frequency ν_t for jumps between sites on top of the island.

[3]To keep the notation simple, we have not introduced a new coefficient D' for adatom diffusion in the second layer, which, of course, can be different from D in the first layer.

before the step edge barrier is eventually passed (if no second-layer nucleation occurs). Accordingly,

$$\tau_n(R) = \frac{1}{n}\tau_1(R) = \frac{1}{n}\left(\kappa_1 \frac{R^2}{D} + \kappa_2 \frac{Ra}{WD}\right). \tag{27}$$

Equations (26) and (27) have been validated by more detailed analytical calculations and tested against KMC simulations by Heinrichs, Rottler, and Maass (2000), where, in particular, the constants κ_1 and κ_2 were determined and κ_e was shown to depend on i due to memory effects.

Knowledge of $\tau_n(R)$ allows us to calculate the probabilities $p_n = p_n(R(t))$ of finding n adatoms on top of the island at a time t before the onset of second-layer nucleation. These are given by the Poisson distribution

$$p_n(R) = \frac{\bar{n}(R)^n}{n!}\exp[-\bar{n}(R)], \tag{28}$$

where an analytical expression for the mean number $\bar{n} = \bar{n}(R(t))$ of adatoms was derived by Heinrichs, Rottler, and Maass (2000). It holds that $\bar{n}(R) = \pi F R^2 \tau_1(R)$, except for a regime of small $R/a \ll W^{-1}\Gamma^{-2/(i+2)}$.

With the encounter rates $\omega_n(R)$, the lifetimes $\tau_n(R)$, and the probabilities $p_n(R)$, the second-layer nucleation rate can be evaluated. Different from what one may intuitively expect, it is possible that second-layer nucleation sets in at times when $\bar{n}(R(t)) \ll i+1$, which means when on average less than $i+1$ adatoms are on top of the island (Rottler and Maass, 1999). In this case the nucleation is caused by fluctuations, where by chance $i+1$ adatoms are on top of an island and encounter each other to form a stable nucleus.

To calculate the corresponding fluctuation-dominated nucleation rate $\Omega_{\rm fl}(R)$, consider the probability of a second-layer nucleation event in a finite time interval Δt.[4] This equals the probability $p_i(R(t))$ of finding i atoms on top of the island (states with $n > i$ can be neglected in the fluctuation-dominated situation), times the probability $\pi F R^2 \Delta t$ to deposit an additional atom on the island, times the probability $(1 - \exp[-\omega_{i+1}(R)\tau_{i+1}(R)])$ that $i+1$ adatoms encounter each other during the lifetime $\tau_{i+1}(R)$. Dividing the probability of a nucleation event in Δt by Δt yields

$$\Omega_{\rm fl}(R) = \pi F R^2 \frac{\bar{n}(R)^i}{i!} e^{-\bar{n}(R)}(1 - e^{-\omega_{i+1}(R)\tau_{i+1}(R)}). \tag{29}$$

For $i = 1$, Eqs. (26) and (27) give $\omega_2(R)\tau_2(R) \sim 1/RW$ for $RW \ll 1$ and $\omega_2(R)\tau_2(R) \sim$ const for $RW \gg 1$, which means that the encounter probability $(1 - \exp[-\omega_2(R)\tau_2(R)])$ in Eq. (29) is always of the order of 1. One thus obtains

$$\begin{aligned}\Omega_{\rm fl}(R) &\sim FR^2\bar{n}(R) \sim F^2R^4\tau_1(R) \\ &\sim \begin{cases} FW^{-1}\Gamma^{-1}R^5, & \Gamma^{-11/12} \ll WR \ll 1, \\ F\Gamma^{-1}R^6, & 1 \ll WR. \end{cases}\end{aligned} \tag{30}$$

For $WR \ll \Gamma^{-11/12}$ it holds that $\Omega_{\rm fl}(R) \sim F\Gamma^{-1/3}R^6$.

If $\bar{n}(R(t)) \gtrsim i+1$ at the onset of second-layer nucleation, the rate follows from the weighted sum of the encounter rates $\omega_n(R)$ over all states with $n \geq (i+1)$,

$$\Omega_{\rm mf}(R) = \sum_{n=i+1}^{\infty} p_n(R)\omega_n(R) = \kappa_e \frac{D}{a^2}\bar{n}(R)^{i+1}\left(\frac{a^2}{\pi R^2}\right)^i. \tag{31}$$

This agrees with the result of mean-field theory (Tersoff, Denier van der Gon, and Tromp, 1994), which predicts that $\Omega(R)$ is given by an integration of the local nucleation rate $Dn_1^{i+1} \sim D[\bar{n}(R)/\pi R^2]^{i+1}$ over the island area (factor πR^2).

With a self-consistent analysis it can be decided which of the two different situations leading to Eqs. (29) and (31) actually occurs. Assume that the fluctuation-dominated situation is relevant. Then calculating $f(t)$ from Eq. (25) with $\Omega(R) = \Omega_{\rm fl}(R)$ from Eq. (29), and determining R_c, one can check if $\bar{n}(R_c) \ll i+1$. If this is true, the assumption of a fluctuation-dominated nucleation was correct, while otherwise the mean-field rate from Eq. (31) must be used. When $R(t)$ evolves according to the natural growth law $(FN^{-1}t)^{1/2} \sim F^{1/2}\Gamma^{i/2(i+2)}t^{1/2}$, it turns out that for $i \leq 2$ the fluctuation-dominated rate $\Omega_{\rm fl}(R)$ is relevant, while for $i > 2$ it is the mean-field rate $\Omega_{\rm mf}(R)$ (Heinrichs, Rottler, and Maass, 2000).

With respect to the dependence of R_c on W and Γ the theory based on Eq. (29) predicts various scaling regimes in different intervals of W, where $R_c \sim W^\eta\Gamma^\gamma$ with exponents η and γ depending on i. For example, for $i = 1$, one finds $R_c \sim W^{1/7}\Gamma^{4/21}$ for $W^{(1)} \ll W \ll W^{(2)}$, where $W^{(1)} \sim \Gamma^{-3/4}$ and $W^{(2)} \sim \Gamma^{-1/6}$. The occurrence of the different regimes and their scaling properties were confirmed by KMC simulations (Rottler and Maass, 1999; Heinrichs, Rottler, and Maass, 2000).

In extensions of this theory, more complicated cases of second-layer nucleation can also be treated, including the presence of metastable clusters and of interaction effects between adatoms (Heinrichs, Rottler, and Maass, 2000; Heinrichs and Maass, 2002). Moreover, the same type of fluctuation effects as discussed here leads to a failure of mean-field rate equations for describing chemical reaction kinetics in confined geometries, as, for example, hydrogen recombination on interstellar dust grains. Similar scaling arguments can be used to tackle this related problem (Krug, 2003).

B. Applications

The theory of second-layer nucleation allows one to determine phase diagrams where, depending on the two parameters Γ and W, it is predicted whether films grow into smooth or rough topographies. While such phase diagrams have been validated by KMC simulations (Rottler and Maass, 1999), corresponding experimental studies are still lacking. For a given adsorbate and substrate, different paths in the W-Γ diagram could be explored by changing the flux F and the temperature T. Care would be needed in analyzing such studies because changes in i can go along with changes of T.

A further application of second-layer nucleation theory is the determination of step edge barriers from measurements of the fraction of covered islands. This supplements other techniques as field ion microscopy (Kellogg, 1994), which can suffer from the problem that step edges are not resolved with a sufficient resolution. With STM Bromann *et al.* (1995a)

[4]The interval Δt should be large compared to ω_{i+1}^{-1} and small compared to time scales of changes of $R(t)$.

analyzed the fraction of covered islands in homoepitaxial and heteroepitaxial Ag growth on Ag(111) and Pt(111). They first generated size-tailored Ag islands with a narrow size distribution around a mean radius R_0 by deposition of 10% of a monolayer and subsequent annealing. Different R_0 in the range 10–100 Å were obtained for different annealing times. After a subsequent evaporation of again 10% of a monolayer at different temperatures, the fraction of covered islands $f(R_0)$ as a function of the initial radius R_0 was determined, as shown in Fig. 7 for Ag growth on Pt(111). In this system $i = 1$ below 90 K (Brune *et al.*, 1994). When assuming $\nu_s = \nu_t$, an analysis of the measured $f(R_0)$ with the fluctuation-dominated rate $\Omega_{\rm fl}(R)$ from Eq. (30) yields $\Delta E_{\rm ES} \simeq 43$ meV, while the mean-field rate $\Omega_{\rm mf}(R)$ would give a too small value of $\Delta E_{\rm ES} \simeq 30$ meV. When taking into account interactions in the form of additional ring barriers between mutually approaching adatoms, as predicted by density functional theory (DFT) calculations of Fichthorn and Scheffler (2000), a value $\Delta E_{\rm ES} \simeq 48$ meV is obtained [for details, see Heinrichs and Maass, 2002].

In the case of rough multilayer growth, an alternative way for determining $\Delta E_{\rm ES}$ is to measure the mean radius $R_{\rm top}$ of the top terrace after mound formation in the so-called "wedding cake regime" (Politi, 1997). During mound growth (see Fig. 8), the rate F of creating a new layer should balance the rate of creating a new nucleus on the top terrace, which yields $\Omega(R_{\rm top}) \simeq F$ as a simple determining equation for $R_{\rm top}$. Krug (2000) refined this argument, developed an analytical theory for the size distribution of top terraces, and applied this theory to the mound formation of Pt on Pt(111) shown in Fig. 8.

A strength of the theory of second-layer nucleation is that it does not depend on microscopic details of the interlayer transport. What counts is that there is an *effective* barrier $\Delta E_{\rm ES}$ that hinders the escape of particles from an island. This generality was demonstrated by Hlawacek *et al.* (2008) who applied the theory to mound formation of rodlike

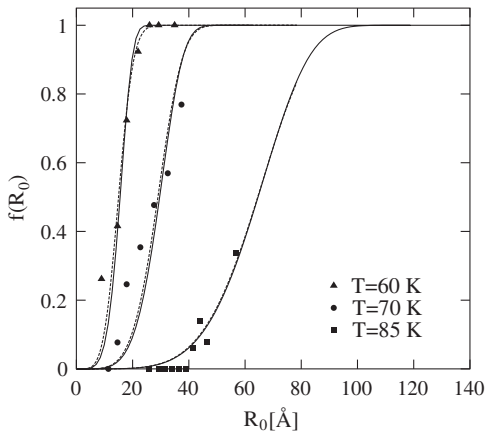

FIG. 7. Fraction of covered islands after deposition of 10% of a monolayer of Ag on a Pt(111) surface with size-tailored islands of mean radius R_0 at three different temperatures ($i = 1$). The symbols refer to the measured data by Bromann *et al.* (1995b), and the solid and dashed lines (almost identical) refer to fits with the second-layer nucleation theory under neglect [see Eq. (29) or (30)] and inclusion of additional ring barriers between mutually approaching adatoms, respectively. From Heinrichs and Maass, 2002.

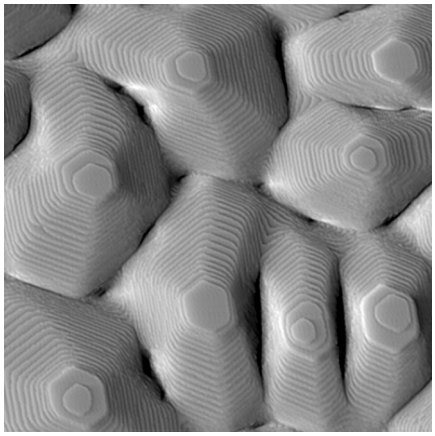

FIG. 8. STM image of mound formation of Pt after deposition on Pt(111). From Krug, Politi, and Michely, 2000.

para-sexiphenyl molecules in organic thin-film growth. Upon deposition of these molecules on an ion-bombarded mica surface these molecules are going to stand upright on the surface with some tilt angle. By analyzing $R_{\rm top}$ for films with large thicknesses a value $\Delta E_{\rm ES} \simeq 0.67$ eV was determined by using the stochastic theory with $i = 1$ in this case. Using a molecular model, they showed that a large contribution to this effective barrier stems from the bending of a molecule when it slides down a step edge, a mechanism very different from those responsible for $\Delta E_{\rm ES}$ in metal epitaxy. For the first molecular layers a lower value $\Delta E_{\rm ES} \simeq 0.26$ eV was determined based on an analysis of the critical radius R_c. This lower value could be traced back to a smaller tilt angle of the molecules in the first layers and an associated lowering of the bending barrier (Hlawacek *et al.*, 2008).

Extension of second-layer nucleation theories to multicomponent systems is an open problem. Differing mobilities in the second layer and differing step edge barriers of the components are expected to give rise to interesting new effects. For example, under codeposition of two species with high and low $\Delta E_{\rm ES}$, the species with higher $\Delta E_{\rm ES}$ should enrich on top of the islands. Accordingly island compositions will depend on temperature and fluxes. In later stages of growth this may lead to compositional profiles that are tunable by experiment.

The essential insight from this section is that for small critical island sizes $i \leq 2$ second-layer nucleation relies on rare fluctuations in the number of adatoms on top of the island, which occur within a time domain where $\bar{n}(R(t)) \ll i + 1$. A stochastic theory capturing theses fluctuations reveals a nucleation rate differing from mean-field predictions. Fitting that theory to metal and organic growth experiments can yield pronounced corrections to the step edge barriers $\Delta E_{\rm ES}$ when compared with predictions from mean-field theory. The criterion distinguishing between 3D island and smooth surface growth will be modified accordingly.

VI. WHAT DETERMINES OUTER SHAPE AND INNER STRUCTURE OF ISLANDS?

At thermodynamic equilibrium, cluster shapes for a given cluster size are governed by the principle of minimal

interfacial free energy, which involves the familiar Wulff construction (Wulff, 1901). For two-dimensional islands on surfaces, it is the step free energy that enters. Under nonequilibrium conditions, cluster shapes are controlled by atomic or molecular moves at or near the cluster surface. When attaching to a cluster, adatoms can encounter many different environments such as facets, edges, kinks, corners, etc., with associated changes of elementary jump energies. This leads to a large variety of outer shapes and inner configurational arrangements. In the following we discuss some key mechanisms for this kinetically controlled structure formation.

A. Island shapes on (111) surfaces

Shapes of two-dimensional islands on (111) surfaces were studied for various systems in metal epitaxy, as for Pt/Pt(111) (Brune *et al.*, 1996), Ag/Pt(111) (Hohage *et al.*, 1996), Al/Al (111) (Ovesson, Bogicevic, and Lundqvist, 1999), Ag/Ag (111) (Cox *et al.*, 2005), and Au/Pt(111) (Ogura *et al.*, 2006). They are widely known and well understood examples of island structures controlled by nonequilibrium kinetics.

At high temperature, edge and corner diffusion are generally fast enough to create sharp island edges (''line facets''). However, different from what one may intuitively expect, islands typically do not exhibit hexagonal but triangular shapes, which implies a breaking of the hexagonal symmetry of the (111) substrate lattice.

To understand this, one must notice that two boundary steps of a hexagon, which meet at one corner, are geometrically inequivalent relative to the substrate. These are often designated as *A* and *B* steps, and the distinction between both becomes clear from Fig. 9(a). If diffusion properties with respect to these different step types are the same, islands assume a hexagonal shape. Differences in the diffusion properties originate primarily from three sources: (i) Stronger binding of adatoms to, say, *A* steps. Attaching adatoms then have a tendency to enrich at *A* steps (Jacobsen, Jacobsen, and Norskov, 1996). (ii) Same binding energy, but faster diffusion of adatoms along *A*, caused by a lower energy barrier (Michely *et al.*, 1993). This leads to a faster nucleation of new atomic rows at *A* steps (Michely and Krug, 2004). (iii) Asymmetric corner diffusion, which means that a onefold coordinated adatom at a corner site goes preferentially to, say, *A* steps. Also this effect leads to an enrichment of atoms at *A* steps. In all these cases, further atoms are thus accumulating faster at one step type, chosen as the *A* step here, and as a consequence the *B* steps grow at the expense of *A* steps. Eventually triangular islands with prevailing *B* steps form.

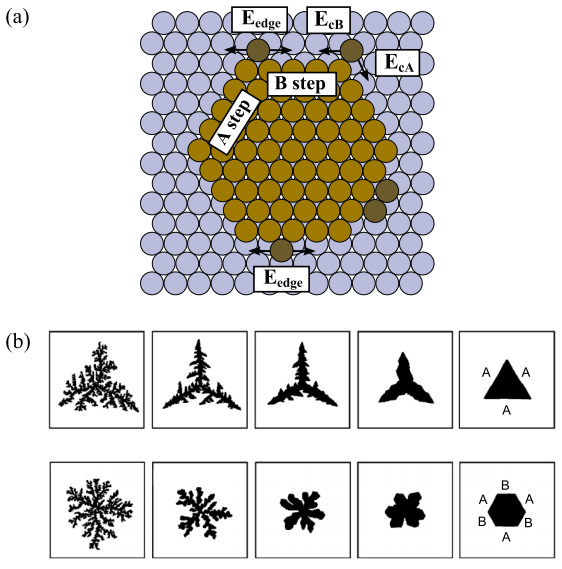

FIG. 9 (color online). (a) Sketch of atomic movements and energy barriers involved in diffusion processes along and between island edges of *A* and *B* type on a (111) surface. (b) Simulated island shapes for $T = 300$ K, $F = 10^{-3}$ ML/s, and the barrier for edge diffusion E_{edge} decreasing from left to right. In the upper panel, corner diffusion is anisotropic with $E_{cB} = 0.1 < E_{cA} = 0.25$ eV, while in the lower panel, corner diffusion is symmetric with $E_{cB} = E_{cA} = 0.11$ eV. Adapted from Ogura *et al.*, 2006.

At low temperatures, the strong binding of atoms favors an aggregation of hit-and-stick type, which leads to fractal-dendritic island shapes. The overall symmetry and ramification of these structures depend again on corner and edge diffusion properties. A demonstration of edge and corner diffusion effects was given by Ogura *et al.* (2006); see Fig. 9(b). For the islands shown in the upper panel of Fig. 9, corner diffusion is asymmetric with activation energies $E_{cB} < E_{cA}$ [cf. Fig. 9(a)], while the island shapes in the lower panel refer to a situation of symmetric corner diffusion. From left to right the barrier E_{edge} [cf. Fig. 9(a)] for edge diffusion (along both *A* and *B* steps) is lowered in both panels. With decreasing E_{edge}, attaching atoms can diffuse over longer distances along the edges and find more favorable binding sites with higher coordination. As a consequence, the structures become less ramified and the side arms thicken with decreasing E_{edge}. In the sequence of structures a skeleton dendrite appears, which has triangular or hexagonal symmetry for asymmetric or symmetric corner diffusion before eventually the compact triangular or hexagonal shape is formed at even lower E_{edge}. Note that an overall triangular or hexagonal symmetry is also visible for the island shapes simulated with large E_{edge}.

It is also possible to obtain compact island shapes with curved edges, if corner diffusion is suppressed (Brune, 1998). By comparison with measurements, features such as the thickness of side branches or the degree of ramification and further details of compact island shapes can be used to identify kinetic parameters in specific models for local diffusion at island boundaries (Michely and Krug, 2004).

B. Second-layer induced morphologies

The second-layer occupation can have a significant influence on the shape and morphology of islands in the first layer. For example, the *A* and *B* steps on (111) surfaces give rise to different step edge barriers in the second layer. The downward fluxes across *A* and *B* steps hence differ, which modifies the in-plane aspect ratio for island shapes (Li *et al.*, 2008).

Quite unexpected complex morphologies can arise due to upward transitions from the first to the second layer on weakly interacting substrates. Such morphologies were recently found for fullerene (C_{60} molecules) adsorbed on ionic surfaces (Burke *et al.*, 2007; Burke, Topple, and Grütter,

2009; Loske *et al.*, 2010). Figure 10 shows AFM images of the self-assembly of C_{60} after deposition on $CaF_2(111)$. At high temperatures [see Figs. 10(a) and 10(d)] triangular islands form that are two monolayers high [see Fig. 10(g)], while at lower temperatures islands with an overall hexagonal shape emerge [see Figs. 10(b), 10(c), 10(e), and 10(f)] that have a base of one monolayer [see Fig. 10(h)] and exhibit a complicated structure with double-layer rims at the island edges and channels directed toward the interior of the islands. These low-temperature morphologies are very different from the fractal-dendritic island shapes found in metal epitaxy.

The emergence of these morphologies can be understood from a mechanism of facilitated dewetting (Körner *et al.*, 2011). Facilitated dewetting means that a C_{60} molecule on an edge site in the second layer lowers the energy barrier for an upward transition of another molecule to a neighboring edge site in the second layer. At high temperatures a first upward transition over a bare dewetting barrier typically occurs early during growth of an island, when it consists of only a few C_{60} molecules. C_{60} molecules in the second layer subsequently lower the energy barrier for further upward transitions to neighboring sites, and as a consequence islands grow as double layers. The fact that these double-layer islands evolve into triangular rather than hexagonal shapes has its origin, similar to the island growth on (111) surfaces in metal epitaxy (cf. Sec. VI.A), in a symmetry breaking effect associated with *A* and *B* steps. The distinction between these steps has no meaning here for monolayer islands because of the large diameter of the C_{60} molecules compared to the lattice constant of the $CaF_2(111)$ substrate. The two types of steps can be distinguished, however, in the second layer. As illustrated in Fig. 11, upward transitions of C_{60} at *A* steps are more frequent than at *B* steps, because they require only two rather

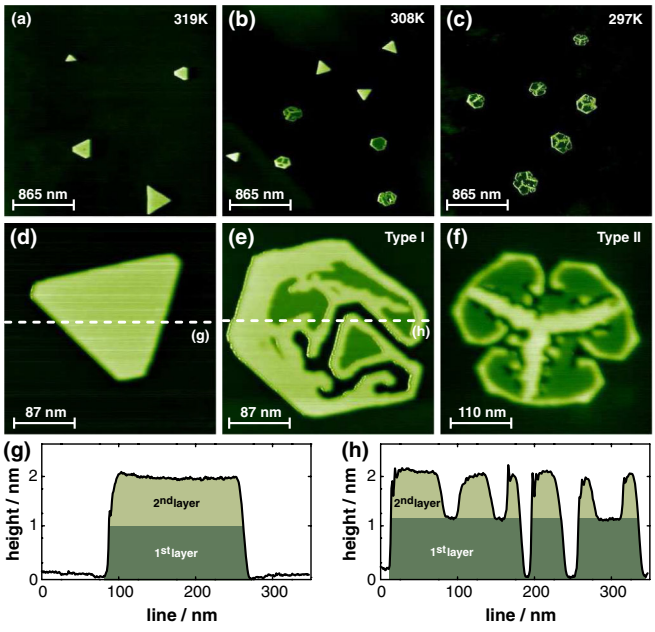

FIG. 10 (color online). (a)–(c) AFM images of C_{60} islands on $CaF_2(111)$ at three different growth temperatures. (d)–(f) Magnified images of single islands: a compact triangle (d), and hexagonal islands with morphologies I (e) and II (f). (g), (h) Height profiles along line scans shown in (d) and (e). From Körner *et al.*, 2011.

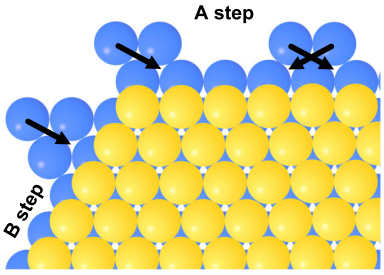

FIG. 11 (color online). Sketch of elementary upward jump processes facilitating the growth of a double-layer triangle. The processes at the *A* step and the corner between the *A* and *B* step involve only two C_{60} and are, therefore, more likely than the process at the *B* step involving three C_{60} molecules. From Körner *et al.*, 2011.

than three C_{60} molecules in the first layer. Accordingly, triangular shapes with prevailing *B* steps result.

At low temperatures upward transition of C_{60} over the bare dewetting barrier becomes rare events and large islands with overall hexagonal shape form. For these large islands, deposition on top of islands is the dominating process of second-layer occupation with nucleation kinetics as described in Sec. V (for $i = 1$ and large step edge barriers). An island initially one layer high can evolve into two different types of morphologies I and II, depending on whether the first stable cluster of C_{60} in the second layer is nucleated close to an edge or close to the center of the island.

Growth of a stable second-layer cluster close to the island boundary soon leads to a contact with an edge, which triggers the process of facilitated dewetting. Starting from the point of contact, double-layer rims are growing along the island edges due to facilitated upward transitions of C_{60}. During the period of C_{60} deposition, these rims do not succeed in surrounding the island, because the island area extends faster by newly attaching C_{60} to the rim-free edges than to the edges with rim, where facilitated dewetting leads to a broadening of the rim. In the postdeposition regime, however, the ends of the rim grow farther by facilitated upward transitions of C_{60} that stem from the rim-free edges and diffuse along the island edges. If the two ends of the rim eventually approach each other along the same edge, a funnel starts to form and further growth of this funnel leads to a trench extending toward the interior of the island together with the rim. This leads to morphology I with a typical example shown in Fig. 10(e).

If a stable second-layer cluster nucleates close to the island center, a dendritic-skeletal cluster shape evolves, which resembles the simulated morphology in the second-to-last structure (from left to right) of the upper panel of Fig. 9(b). In the postdeposition period the skeletal dendrite grows very slowly by rare upward transitions of C_{60} over the bare dewetting barrier until one of the three finger tips reaches an island edge. At this moment facilitated dewetting transitions set in and a rim starts to grow along both sides of the finger terminus at the island edge. The formation of the rim is accompanied by a loss of C_{60} molecules at the rim-free edges causing one of the two other finger tips of the dendrite to reach an island edge. A rim then starts to grow also from this finger terminus and thereafter also the third finger tip reaches the island edge with subsequent rim formation. Eventually the

three growing rims move toward each other close to edge points located halfway between the tip termini, where funnels form and subsequently trenches grow toward the island interior. As a result, morphology II with an approximate threefold symmetry is obtained with a typical example shown in Fig. 10(f).

All these complicated structures found in experiment were successfully modeled by a kinetic growth model based on the mechanism of facilitated dewetting (Körner *et al.*, 2011).

C. Segregation and ordering effects

Questions concerning the inner structure of clusters are most relevant for 3D binary systems, produced by codeposition of different atomic species. Compositional fluctuations in these systems are characterized primarily in terms of atomic short- or long-range order in the cluster's interior, and in terms of surface segregation, i.e., in the enrichment of one atomic species at the cluster surface. At equilibrium these two features generally compete with each other (Polak and Rubinovich, 2000). This can be understood intuitively because strong ordering interactions inside the "bulk" will enforce atomic order up to the surface and hence impede surface segregation. Conversely, surface interactions favoring segregation will suppress ordering tendencies, at least in the near-surface region.

For cluster growth outside equilibrium, these arguments remain qualitatively valid, but the degree of ordering and segregation diminishes. Although atomic diffusion, necessary for equilibration, is often frozen in the bulk, some remanent bulk order can develop, as a result of previous diffusion steps of surface atoms before being buried by the external flux. So the question arises: What kind of metastable compositional fluctuations are generated below the advancing surface of a 3D nanocluster under the condition of active surface but frozen bulk kinetics?

Theoretically, the relationship between surface kinetics and emerging frozen bulk structure has remained largely unexplored. Some aspects were recently studied with the help of an analytically solvable model for 1D growth (Einax and Dieterich, 2008). Quite obviously, remanent bulk order depends on the ratio between the time scales for surface diffusion and atomic deposition. Coming from high temperatures, ordering will initially improve upon cooling, but near some blocking temperature, where those two time scales match, it will pass a maximum and drop down to zero as $T \to 0$ (see Fig. 12 for an example). In this limit both bulk and surface kinetics get frozen, leading to random compositions.

Particularly interesting is the structure of alloy clusters with magnetic components. Attempts to generate perpendicular magnetic anisotropy (PMA), where the easy axis of magnetization is perpendicular to the substrate plane, have received special attention. This requires the magnetocrystalline perpendicular anisotropy to be stronger than the shape anisotropy due to dipolar interactions, which generally favor in-plane magnetization. PMA is well known to occur in multilayer films (Johnson *et al.*, 1996) and has been exploited to increase storage capacities in magnetic devices. Its occurrence in nanoclusters was detected, for example, in FePt or

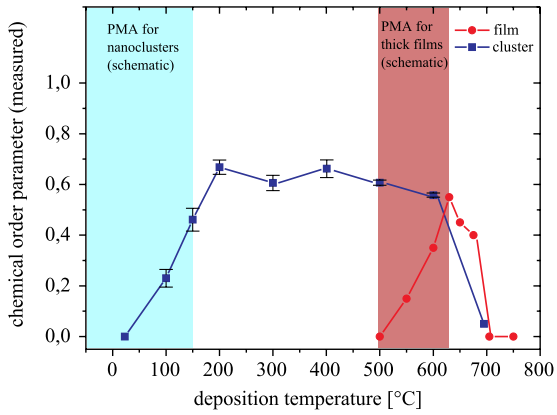

FIG. 12 (color online). Chemical order for $CoPt_3$ clusters (grains) grown on $WSe_2(0001)$ and $CoPt_3$ films grown on Pt(111) as a function of the growth temperature. $L1_2$-type ordering sets in below the bulk disorder or order transition temperature $T \simeq 686\,^{\circ}\mathrm{C}$, and vanishes at lower temperatures when the bulk kinetics becomes frozen. For clusters, the vanishing of $L1_2$-type ordering occurs at a lower temperature because atomic rearrangements at the advancing surface allow some degree of chemical order in the interior to be built. The occurrence of PMA is schematically indicated for both clusters and films. Adapted from Maier *et al.*, 2002.

CoPt alloy clusters. Depending on the technique and on the conditions of growth, the experiments suggest an anisotropic short-range (Liscio *et al.*, 2010) or layer $L1_0$-type long-range order (Zeng *et al.*, 2002; Andersson *et al.*, 2006; Moulas *et al.*, 2008; Perumal *et al.*, 2008) to be associated with the PMA.

Magnetocrystalline anisotropies are caused by quantum-mechanical effects, which lead to a preferential alignment of magnetic moments along symmetry directions in the crystal lattice. Most important are hybridization of d electron states between neighboring atoms and a strong spin-orbit coupling. A theoretical description requires sophisticated *ab initio* calculations for the electronic structure together with the Dirac equation to include relativistic effects [see, e.g., Šipr *et al.* (2010)].

To get an understanding of the connection between the compositional structure of clusters and the occurrence of PMA, one can adopt a simplified bond picture (Néel, 1954; Victora and MacLaren, 1993). For an AB binary alloy nanocluster with vacancies V the magnetocrystalline anisotropy energy is then expressed as

$$H_{\mathcal{A}} = -\sum_{\langle i,j\rangle}\sum_{\alpha,\beta} \mathcal{A}_{\alpha\beta}(\hat{\boldsymbol{\mu}}_i^{\alpha}\cdot\hat{\boldsymbol{\delta}}_{ij})^2 m_i^{\alpha} m_j^{\beta}, \tag{32}$$

where the sum runs over all cluster sites i and their nearest-neighbor sites j, connected by bond vectors $\boldsymbol{\delta}_{ij}$; m_i^{α} are occupation numbers ($m_i^{\alpha} = 1$ if site i is occupied by species α or zero else, $\alpha = A, B, V$), and $\boldsymbol{\mu}_i^{\alpha}$ are the magnetic moments ($\boldsymbol{\mu}_i^{V} = 0$); $\hat{\boldsymbol{\delta}}_{ij}$ and $\hat{\boldsymbol{\mu}}_i^{\alpha}$ designate unit vectors. The parameters $\mathcal{A}_{\alpha\beta}$ quantify the magnetic anisotropy energies for moments $\boldsymbol{\mu}_i^{\alpha}$ associated with an occupation of neighboring sites by β species. They can be estimated from experiments or determined from *ab initio* calculations. Note that Eq. (32) represents the lowest order term of an expansion in

powers of magnetic moments implied by symmetry arguments.

Using Eq. (32), the structural magnetic anisotropy energy of a fully magnetized cluster is given by $E_{\rm str} = H_{\mathcal{A}}\{\text{all } \boldsymbol{\mu}_i^{\alpha} \text{ in plane}\} - H_{\mathcal{A}}\{\text{all } \boldsymbol{\mu}_i^{\alpha} \text{ out of plane}\}$. This can be reduced to calculating the numbers $n_{\parallel}^{\alpha\beta}$ and $n_{\perp}^{\alpha\beta}$ of in-plane and out-of-plane α-β bonds with direction parallel to the substrate and with components perpendicular to it, respectively.

The procedure has been applied to study the occurrence of PMA for chemically disordered $CoPt_3$ clusters, which were grown on a van der Waals substrate (Albrecht *et al.*, 2001, 2002). These clusters are at low temperature in a metastable state, where the formation of $L1_2$-type chemical order is kinetically suppressed. PMA occurs below and near the onset of $L1_2$ ordering; see Fig. 12. As observed for films, one can expect that this PMA vanishes for even lower temperatures and hence occurs in a temperature window. Using values reported for Co and Pt moments as well as experimental results for Co-Pt multilayers and theoretical results for the Co-vacuum interfaces, one can estimate that the dominant contribution in Eq. (32) comes from Co-Pt bonds with $\mathcal{A}_{\rm CoPt} \simeq 250\ \mu$eV, and accordingly $E_{\rm str} \propto n_{\perp}^{\rm CoPt} - n_{\parallel}^{\rm CoPt}$ (Heinrichs, Dieterich, and Maass, 2007). Taking into account the strong surface segregation of Pt caused by its larger size compared to Co (Gauthier *et al.*, 1992), a mechanism for the PMA as depicted in Fig. 13 is conceivable. At low T, flat clusters with extended top and small side facets occur and surface segregation is kinetically suppressed. At high T the side facets become comparatively large. Depending on details of the interactions, an intermediate temperature range can exist, where the cluster is still fairly flat and the surface segregation is sufficiently strong. In this case the contribution to the magnetic anisotropy energy coming from the out-of-plane Co-Pt bonds at the top facet can be larger than the contribution from the in-plane Co-Pt bonds at the side facets. Accordingly, PMA is expected to occur.

Indeed, this mechanism for the occurrence of PMA could be corroborated by KMC simulations of an AB_3 alloy with nearest-neighbor interactions V_{AA}, V_{BB}, and V_{AB} adjusted to equilibrium properties of $CoPt_3$ (Heinrichs, Dieterich, and Maass, 2006, 2007). The substrate was modeled by a weak attractive substrate potential. Growth of the clusters in time proceeds by codeposition of Co and Pt atoms, vacancy-assisted nearest-neighbor hopping, and by direct exchange between unlike low-coordinated atoms on top of terraces or step edges. Such direct exchange processes are often observed in heteroepitaxial growth, and, in particular, were seen for Co deposited on Pt(111) (Gambardella *et al.*, 2000; De Santis *et al.*, 2002). As the model is fully three dimensional, interlayer diffusion and Ehrlich-Schwoebel barriers are automatically taken into account.

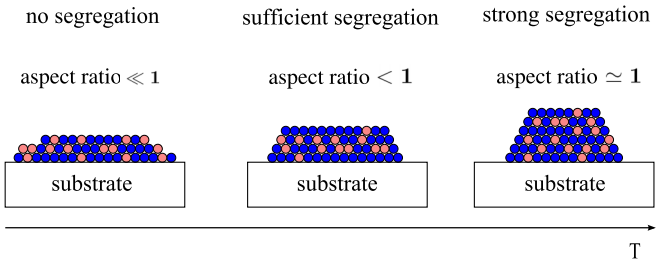

FIG. 13 (color online). Sketch of changes in the structure and shape of binary alloy nanoclusters (e.g., $CoPt_3$) with temperature. Atoms of the two components are marked (light) (e.g., Co) and (dark) (e.g., Pt), where the latter tend to segregate at the cluster surface. With increasing T the fraction of side facets increases relative to the top facet and the surface segregation becomes stronger. The two competing effects for PMA lead to a temperature window of its occurrence.

Figure 14 shows model results for the magnetic anisotropy energy, both for its structural contribution $E_{\rm str}$ and for the total energy $E_{\rm tot} = E_{\rm str} + E_{\rm dip}$ obtained by adding the (negative) dipolar contribution. The maximum $E_{\rm str} \simeq 40$ meV at $T \simeq 145\,^{\circ}$C was shown to originate from the interplay of Pt surface segregation, facilitated by direct exchange processes, with T-dependent cluster shapes. It hence reflects the mechanism sketched in Fig. 13 so that PMA indeed is a surface effect.

Simulations with varying cluster size N show that $E_{\rm str} \propto N^{2/3}$, so that PMA indeed is a surface effect. The N dependence of the total anisotropy energy therefore is given by

$$E_{\rm tot} = E_{\rm str} + E_{\rm dip} = K_{\rm str}N^{2/3} - K_{\rm dip}N \tag{33}$$

with anisotropy constants $K_{\rm str}$ and $K_{\rm dip}$. Equation (33) was shown to represent the KMC data very well. It predicts an optimal mean cluster size, where PMA is strongest, and a critical mean cluster size, above which the magnetization switches to an in-plane orientation (when $E_{\rm tot} < 0$). These predictions have yet to be confirmed in experiments. For cluster sizes $N \simeq 1200$, as used in the measurements by Albrecht *et al.* (2001), $E_{\rm tot}$ calculated from the model has the right order of magnitude when compared with the experimental one. Also shown in Fig. 14 is the structural order parameter for $L1_2$ ordering, which quantifies the preferential occupation of one of the four simple cubic sublattices of the fcc lattice by Co atoms. While $L1_2$ ordering remains kinetically suppressed up to room temperature, it becomes

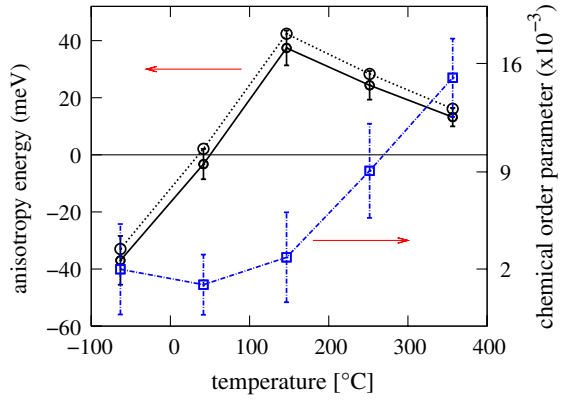

FIG. 14 (color online). Magnetic anisotropy energies $E_{\rm tot}$ (solid line), $E_{\rm str}$ (dotted line), and the chemical order parameter (dash-dotted line) vs temperature of simulated $CoPt_3$ nanoclusters with 1000 atoms for strong surface segregation of Pt ($V_{\rm PtPt} - V_{\rm CoCo} = 180$ meV) and high exchange rates of Co and Pt at the cluster surface. Adapted from Heinrichs, Dieterich, and Maass, 2007.

significant only at higher temperatures, where PMA has already passed its maximum. These trends obviously agree with the experimental behavior displayed in Fig. 12.

We remark that measurements of the local order in $CoPt_3$ nanostructures on a van der Waals substrate confirmed preferential Co-Pt and Co-Co binding out of plane and in plane as the origin of PMA at room temperature (Liscio *et al.*, 2010), but in addition uncovered structural details which go beyond the above model. We further note that Maranville, Schuerman, and Hellman (2006), using simulations on a more microscopic level, were able to interpret PMA in ultrathin continuous $CoPt_3$ films occurring at elevated temperatures in terms of Co segregation along step edges.

In this section our main focus was on examples of unexpected cluster shape and structure formation, as discovered in recent experiments. Specific mechanisms were identified that can explain these experiments. For fullerenes (C_{60}) adsorbed on a weakly interacting substrate (see Sec. VI.B), a distinction between A and B steps and anisotropic growth arises through second-layer occupation. This is in contrast to Sec. VI.A, where the distinction between A and B steps is due to the substrate. In turn, a new mechanism of second-layer facilitated dewetting was proposed, which explains the triangular to hexagonal shape transition of fullerene islands, followed in the postdeposition regime by the evolution of complex morphologies.

To reveal the possible origins of PMA in nanoclusters, $CoPt_3$ nanocluster growth on a van der Waals substrate was considered in Sec. VI.C. It turned out that PMA occurs as a result of an anisotropic atomic short-range order in the cluster. Important features in the clusters' atomic structure and their magnetic properties were interpreted by a mechanism based on active surface but frozen bulk kinetics and a concomitant competition between cluster shapes and Pt surface segregation.

VII. CONCLUDING REMARKS

Cluster growth on surfaces is a field that connects fundamental studies of nonequilibrium phenomena with questions related to the development of nanomaterials of practical use. Modern topics such as the growth of organic molecules and of nanoalloys with functional properties make it necessary to reanalyze specific questions which are central to this field. In this Colloquium we summarized basic concepts of surface growth kinetics and showed for a number of examples how these can be extended and further developed to tackle open problems of current interest.

An important basis for describing cluster growth on surfaces is laid by the rate equation approach. Extending this approach to binary alloys or, more generally, to multicomponent adsorbates provides an accurate framework for the analysis of future experiments on the submonolayer kinetics driven by codeposition of two (or more) atomic species. We hope that this framework, presented in Sec. III, will stimulate experimental tests of our findings and eventually will help to control nanoalloy surface growth.

Even for one-component metallic growth the exact behavior of the ISD is still not known, not even in the $D/F \to \infty$ limit. Section IV provides evidence from simulations that rate equations based on "correct" capture numbers do have predictive power for the ISDs. With respect to extensions to multicomponent systems, this feature is expected to remain valid. However, for predicting ISDs from the rate equations, no analytical theory of sufficient accuracy exists so far for the capture numbers. Promising approaches for resolving this problem are theories for joint probabilities of island size and capture area. Further developments of such theories may provide a route also to account for coverage dependencies of scaled ISDs in the $D/F \to \infty$ limit.

Nucleation of stable islands in confined geometries can be dominated by rare fluctuations with the consequence that mean-field-type descriptions fail. This fact is particularly important for the problem of second-layer nucleation when the size of the critical nucleus is one or two (see Sec. V). Stochastic methods developed for treating rare fluctuations proved applicable also to organic thin-film growth, when bending energies are involved in the passing of step edges, and they were useful for making progress in other contexts such as chemical reaction kinetics. There is more to be explored. For example, rare fluctuations should play an important role also for island nucleation on reconstructed surfaces, and different Ehrlich-Schwoebel barriers for different types of atoms should have a relevant influence on island shapes, similar to different barriers associated with A and B steps on (111) surfaces (Evans, Thiel, and Bartelt, 2006).

Alloy cluster formation under nonequilibrium growth conditions allows one to generate new atomic configurations that, while not relaxed in thermal equilibrium, are nevertheless long living due to frozen kinetics. This is of particular interest when materials with new functional properties can be created. An example is the occurrence of PMA in alloy nanoclusters with components carrying magnetic moments (see Sec. VI). It was predicted that PMA can be enhanced when clusters are grown in an external perpendicular magnetic field (Einax, Heinrichs *et al.*, 2007a; 2007b), but this has not yet been confirmed by experiment. For AB_3 alloys, which show $L1_2$-type ordering at equilibrium, this enhancement is expected to be small. It may become significant, however, for AB alloys exhibiting $L1_0$-type ordering, as, for example, CoPt or FePt (Lyubina *et al.*, 2011). At equilibrium, these alloys display a transition to a layer structure with alternating Co (Fe)- and Pt-rich layers. $L1_0$-type ordering implies that the magnetic anisotropy becomes a bulk property, much larger than that in $CoPt_3$. Since the appearance of the $L1_0$ phase requires relatively high annealing temperatures (Perumal *et al.*, 2008; Makarov *et al.*, 2009), the temperature range below the onset of long-range chemical order is of practical interest as well. Regarding growth experiments under such conditions, these materials seem to be promising candidates for detecting a substantial magnetic field-induced enhancement of PMA. More experimental and theoretical studies of the inner structure of metastable alloy clusters grown by atomic deposition appear to be necessary in order to exploit the full potential of these systems in materials science.

For organic thin-film growth, the established concepts of submonolayer growth kinetics should be revisited in order to incorporate intermolecular interaction effects such as π stacking and hydrogen bonding, which are absent in metal and semiconductor adsorbates. In addition, new degrees of

freedom, such as rotation and bending of molecules, need to be considered. Because of orientational constraints for bonding and strong incommensurabilities of molecular sizes (or of sizes of molecular subgroups) with substrate lattice constants, critical nuclei can be composed of quite a large number of molecules. These larger sizes of critical nuclei may be considered as an intermediate case (Schwarz *et al.*, 2012) between the small critical nuclei in metal growth and the large critical nuclei in three-dimensional crystallite formation from solution. Theoretical descriptions of the consequences of these and other features of molecular adsorbates for the growth kinetics are only at the beginning. Novel island morphologies can emerge already due to weak substrate-molecule interactions and an associated upward transport of molecules from the first to the second layer. An unsettled question is to what degree second-layer facilitated dewetting transitions, as found for fullerenes on insulting surfaces, are a rather generic mechanism influencing shapes of molecular clusters.

ACKNOWLEDGMENTS

We have greatly benefited from numerous discussions with our colleagues and collaborators M. Albrecht, S. Heinrichs, M. Körner, A. Kühnle, A. Majhofer, M. Reichling, J. Rottler, and G. Schatz.

REFERENCES

Albrecht, M., M. Maier, F. Treubel, M. Maret, R. Poinsot, and G. Schatz, 2001, Europhys. Lett. **56**, 884.
Albrecht, M., M. Maret, A. Maier, F. Treubel, B. Riedlinger, U. Mazur, G. Schatz, and S. Anders, 2002, J. Appl. Phys. **91**, 8153.
Amar, J. G., and F. Family, 1995, Phys. Rev. Lett. **74**, 2066.
Amar, J. G., M. N. Popescu, and F. Family, 2001, Phys. Rev. Lett. **86**, 3092.
Andersson, G., T. Burkert, P. Warnicke, M. Björck, B. Sanyal, C. Chacon, C. Zlotea, L. Nordström, P. Nordblad, and O. Eriksson, 2006, Phys. Rev. Lett. **96**, 037205.
Antczak, G., and G. Ehrlich, 2010, *Surface Diffusion: Metals, Metal Atoms, and Clusters* (Cambridge University Press, Cambridge, England).
Bales, G. S., and D. C. Chrzan, 1994, Phys. Rev. B **50**, 6057.
Bales, G. S., and A. Zangwill, 1997, Phys. Rev. B **55**, R1973.
Bartelt, M. C., and J. W. Evans, 1992, Phys. Rev. B **46**, 12 675.
Bartelt, M. C., and J. W. Evans, 1996, Phys. Rev. B **54**, R17 359.
Barth, J. V., H. Brune, B. Fischer, J. Weckesser, and K. Kern, 2000, Phys. Rev. Lett. **84**, 1732.
Becker, R., and W. Döring, 1935, Ann. Phys. (Berlin) **416**, 719.
Bromann, K., H. Brune, H. Röder, and K. Kern, 1995a, Phys. Rev. Lett. **75**, 677.
Bromann, K., H. Brune, H. Röder, and K. Kern, 1995b, Phys. Rev. Lett. **75**, 677.
Brune, H., 1998, Surf. Sci. Rep. **31**, 121.
Brune, H., S. Bales, J. Jacobsen, C. Boragno, and K. Kern, 1999, Phys. Rev. B **60**, 5991.
Brune, H., H. Röder, C. Boragno, and K. Kern, 1994, Phys. Rev. Lett. **73**, 1955.
Brune, H., H. Röder, K. Bromann, K. Kern, J. Jacobsen, P. Stoltze, K. Jacobsen, and J. Norskov, 1996, Surf. Sci. **349**, L115.
Burke, S. A., W. Ji, J. M. Mativetsky, J. M. Topple, S. Fostner, H.-J. Gao, H. Guo, and P. Grütter, 2008, Phys. Rev. Lett. **100**, 186104.
Burke, S. A., J. M. Mativetsky, S. Fostner, and P. Grütter, 2007, Phys. Rev. B **76**, 035419.
Burke, S. A., J. M. Mativetsky, R. Hoffmann, and P. Grütter, 2005, Phys. Rev. Lett. **94**, 096102.
Burke, S. A., J. M. Topple, and P. Grütter, 2009, J. Phys. Condens. Matter **21**, 423101.
Castro Neto, A. H., F. Guinea, N. M. R. Peres, K. S. Novoselov, and A. K. Geim, 2009, Rev. Mod. Phys. **81**, 109.
Clancy, P., 2011, Chem. Mater. **23**, 522.
Coraux, J., A. T. N'Diaye, M. Engler, C. Busse, D. Wall, N. Buckanie, F.-J. M. zu Heringdorf, R. van Gastel, B. Poelsema, and T. Michely, 2009, New J. Phys. **11**, 023006.
Cox, E., M. Li, P.-W. Chung, C. Ghosh, T. S. Rahman, C. J. Jenks, J. W. Evans, and P. A. Thiel, 2005, Phys. Rev. B **71**, 115414.
Cuevas, J. C., and E. Scheer, 2010, *Molecular Electronics: An Introduction to Theory and Experiment*, World Scientific Series in Nanoscience and Nanotechnology (World Scientific, Singapore), 1st ed.
Cuniberti, G., G. Fagas, and K. Richter, 2005, *Introducting Molecular Electronics* (Springer, Berlin).
Deibel, C., and V. Dyakonov, 2010, Rep. Prog. Phys. **73**, 096401.
De Santis, M., R. Baudoing-Savois, P. Dolle, and M. C. Saint-Lager, 2002, Phys. Rev. B **66**, 085412.
Dieterich, W., M. Einax, and P. Maass, 2008, Eur. Phys. J. Special Topics **161**, 151.
Ehrlich, G., and F. G. Hudda, 1966, J. Chem. Phys. **44**, 1039.
Einax, M., and W. Dieterich, 2008, New J. Phys. **10**, 103008.
Einax, M., W. Dieterich, and P. Maass, 2009, J. Appl. Phys. **105**, 054312.
Einax, M., S. Heinrichs, P. Maass, A. Majhofer, and W. Dieterich, 2007a, J. Phys. Condens. Matter **19**, 086227.
Einax, M., S. Heinrichs, P. Maass, A. Majhofer, and W. Dieterich, 2007b, Mater. Sci. Eng., C **27**, 1325.
Einax, M., P. Maass, and W. Dieterich, 2013 (unpublished).
Einax, M., S. Ziehm, W. Dieterich, and P. Maass, 2007, Phys. Rev. Lett. **99**, 016106.
Einstein, T. L., and T. J. Stasevich, 2010, Science **327**, 423.
Elder, K. R., M. Katakowski, M. Haataja, and M. Grant, 2002, Phys. Rev. Lett. **88**, 245701.
Elder, K. R., G. Rossi, P. Kanerva, F. Sanches, S.-C. Ying, E. Granato, C. V. Achim, and T. Ala-Nissila, 2012, Phys. Rev. Lett. **108**, 226102.
Evans, J. W., and M. C. Bartelt, 2001, Phys. Rev. B **63**, 235408.
Evans, J. W., and M. C. Bartelt, 2002, Phys. Rev. B **66**, 235410.
Evans, J. W., P. A. Thiel, and M. C. Bartelt, 2006, Surf. Sci. Rep. **61**, 1.
Fichthorn, K. A., and M. Scheffler, 2000, Phys. Rev. Lett. **84**, 5371.
Gambardella, P., M. Blanc, L. Burgi, K. Kuhnke, and K. Kern, 2000, Surf. Sci. **449**, 93.
Ganapathy, R., M. R. Buckley, S. J. Gerbode, and I. Cohen, 2010, Science **327**, 445.
Gao, L., J. R. Guest, and N. P. Guisinger, 2010, Nano. Lett. **10**, 3512.
Gao, M., Y. Pan, L. Huang, H. Hu, L. Z. Zhang, H. M. Guo, S. X. Du, and H.-J. Gao, 2011, Appl. Phys. Lett. **98**, 033101.
Gauthier, Y., R. Baudoing-Savois, J. M. Bugnard, U. Bardi, and A. Atrei, 1992, Surf. Sci. **276**, 1.
Greenwood, M., N. Provatas, and J. Rottler, 2010, Phys. Rev. Lett. **105**, 045702.
Grüneis, A., and D. V. Vyalikh, 2008, Phys. Rev. B **77**, 193401.
Gyure, M. F., C. Ratsch, B. Merriman, R. E. Caflisch, S. Osher, J. J. Zinck, and D. D. Vvedensky, 1998, Phys. Rev. E **58**, R6927.

Heinrichs, S., W. Dieterich, and P. Maass, 2006, Europhys. Lett. **75**, 167.
Heinrichs, S., W. Dieterich, and P. Maass, 2007, Phys. Rev. B **75**, 085437.
Heinrichs, S., and P. Maass, 2002, Phys. Rev. B **66**, 073402.
Heinrichs, S., J. Rottler, and P. Maass, 2000, Phys. Rev. B **62**, 8338.
Hlawacek, G., P. Puschnig, P. Frank, A. Winkler, C. Ambrosch-Draxl, and C. Teichert, 2008, Science **321**, 108.
Hlawacek, G., and C. Teichert, 2013, J. Phys. Condens. Matter **25**, 143202.
Hohage, M., M. Bott, M. Morgenstern, Z. Zhang, T. Michely, and G. Comsa, 1996, Phys. Rev. Lett. **76**, 2366.
Jacobsen, J., K. W. Jacobsen, and J. K. Norskov, 1996, Surf. Sci. **359**, 37.
Johnson, M. T., P. J. H. Bloemen, F. J. A. den Broeder, and J. J. de Vries, 1996, Rep. Prog. Phys. **59**, 1409.
Käfer, D., C. Wöll, and G. Witte, 2009, Appl. Phys. A **95**, 273.
Kellogg, G. L., 1994, Surf. Sci. Rep. **21**, 1.
Körner, M., M. Einax, and P. Maass, 2010, Phys. Rev. B **82**, 201401R.
Körner, M., M. Einax, and P. Maass, 2012, Phys. Rev. B **86**, 085403.
Körner, M., F. Loske, M. Einax, A. Kühnle, M. Reichling, and P. Maass, 2011, Phys. Rev. Lett. **107**, 016101.
Kowarik, S., A. Gerlach, and F. Schreiber, 2008, J. Phys. Condens. Matter **20**, 184005.
Kratzer, P., and M. Scheffler, 2001, Comput. Sci. Eng. **3**, 16.
Krug, J., 2000, Eur. Phys. J. B **18**, 713.
Krug, J., 2003, Phys. Rev. E **67**, 065102.
Krug, J., P. Politi, and T. Michely, 2000, Phys. Rev. B **61**, 14 037.
Kühnle, A., 2009, Curr. Opin. Colloid Interface Sci. **14**, 157.
Landau, D. P., and K. Binder, 2005, *A Guide to Monte Carlo Simulations in Statistical Physics* (Springer, Berlin), 2nd ed.
Li, M., P.-W. Chung, E. Cox, C. J. Jenks, P. A. Thiel, and J. W. Evans, 2008, Phys. Rev. B **77**, 033402.
Li, M., Y. Han, and J. W. Evans, 2010, Phys. Rev. Lett. **104**, 149601.
Liscio, F., M. Maret, C. Meneghini, S. Mobilio, O. Proux, D. Makarov, and M. Albrecht, 2010, Phys. Rev. B **81**, 125417.
Loginova, E., N. C. Bartelt, P. J. Feibelman, and K. F. McCarty, 2008, New J. Phys. **10**, 093026.
Lorbek, S., G. Hlawacek, and C. Teichert, 2011, Eur. Phys. J. Appl. Phys. **55**, 23 902.
Loske, F., J. Lübbe, J. Schütte, M. Reichling, and A. Kühnle, 2010, Phys. Rev. B **82**, 155428.
Lyubina, J., B. Rellinghaus, O. Gutfleisch, and M. Albrecht, 2011, in *Handbook of Magnetic Materials*, edited by K. Buschow (Elsevier, New York), Vol. 19, p. 291.
Maier, A., B. Riedlinger, F. Treubel, M. Maret, M. Albrecht, E. Beaurepaire, J. Tonnerre, and G. Schatz, 2002, J. Magn. Magn. Mater. **240**, 377.
Makarov, D., F. Klimenta, S. Fischer, F. Liscio, S. Schulze, M. Hietschold, M. Maret, and M. Albrecht, 2009, J. Appl. Phys. **106**, 114322.
Maranville, B. B., M. Schuerman, and F. Hellman, 2006, Phys. Rev. B **73**, 104435.
Michely, T., M. Hohage, M. Bott, and G. Comsa, 1993, Phys. Rev. Lett. **70**, 3943.
Michely, T., and J. Krug, 2004, *Islands, Mounds and Atoms: Patterns and Processes in Crystal Growth Far from Equilibrium* (Springer, Berlin).
Moldovan, M. S., H. Bulou, Y. J. Dappe, I. Janowska, D. Bgin, C. Pham-Huu, and O. Ersen, 2012, J. Phys. Chem. C **116**, 9274.
Moulas, G., *et al.*, 2008, Phys. Rev. B **78**, 214424.
Mulheran, P. A., 2004, Europhys. Lett. **65**, 379.
Mulheran, P. A., and D. A. Robbie, 2000, Europhys. Lett. **49**, 617.
Müller, B., L. Nedelmann, B. Fischer, H. Brune, and K. Kern, 1996, Phys. Rev. B **54**, 17 858.
Néel, L., 1954, J. Phys. Radium **15**, 225.
Nicholson, P. G., and F. A. Castro, 2010, Nanotechnology **21**, 492001.
Nitzan, A., and M. A. Ratner, 2003, Science **300**, 1384.
Ogura, S., K. Fukutani, M. Matsumoto, T. Okano, M. Okada, and T. Kawamura, 2006, Phys. Rev. B **73**, 125442.
Oliveira, T. J., and F. D. A. Aarão Reis, 2011, Phys. Rev. B **83**, 201405.
Oliveira, T. J., and F. D. A. Aarão Reis, 2012, Phys. Rev. B **86**, 115402.
Ovesson, S., A. Bogicevic, and B. I. Lundqvist, 1999, Phys. Rev. Lett. **83**, 2608.
Pandey, P. A., G. R. Bell, J. P. Rourke, A. M. Sanchez, M. D. Elkin, B. J. Hickey, and N. R. Wilson, 2011, Small **7**, 3202.
Perumal, A., Y. K. Takahashi, T. O. Seki, and K. Hono, 2008, Appl. Phys. Lett. **92**, 132508.
Pimpinelli, A., and T. L. Einstein, 2007, Phys. Rev. Lett. **99**, 226102.
Pimpinelli, A., and T. L. Einstein, 2010, Phys. Rev. Lett. **104**, 149602.
Pimpinelli, A., and J. Villain, 1998, *Physics of Crystal Growth* (Cambridge University Press, Cambridge, England).
Polak, M., and L. Rubinovich, 2000, Surf. Sci. Rep. **38**, 127.
Politi, P., 1997, J. Phys. I (France) **7**, 797.
Politi, P., and C. Castellano, 2003, Phys. Rev. B **67**, 075408.
Pomeroy, J. M., and J. D. Brock, 2006, Phys. Rev. B **73**, 245405.
Popescu, M. N., J. G. Amar, and F. Family, 2001, Phys. Rev. B **64**, 205404.
Potocar, T., S. Lorbek, D. Nabok, Q. Shen, L. Tumbek, G. Hlawacek, P. Puschnig, C. Ambrosch-Draxl, C. Teichert, and A. Winkler, 2011, Phys. Rev. B **83**, 075423.
Prieto, J. E., J. de la Figuera, and R. Miranda, 2000, Phys. Rev. B **62**, 2126.
Provatas, N., and K. Elder, 2010, *Phase-Field Methods in Materials Science and Engineering* (Wiley, Weinheim).
Rahe, P., M. Kittelmann, J. L. Neff, M. Nimmerich, M. Reichling, P. Maass, and A. Kühnle, 2013, Adv. Mater. (in press).
Rapaport, D. C. 2004, *The Art of Molecular Dynamics Simulation* (Cambridge University Press, Cambridge, England), 2nd ed.
Ratsch, C., and J. A. Venables, 2003, J. Vac. Sci. Technol. A **21**, S96.
Richter, G., and T. Wagner, 2005, J. Appl. Phys. **98**, 094908.
Rojas, G., X. Chen, D. Kunkel, M. Bode, and A. Enders, 2011, Langmuir **27**, 14267.
Rottler, J., and P. Maass, 1999, Phys. Rev. Lett. **83**, 3490.
Ruiz, R., B. Nickel, N. Koch, L. C. Feldman, R. F. Haglund, A. Kahn, F. Family, and G. Scoles, 2003, Phys. Rev. Lett. **91**, 136102.
Rusponi, S., M. Papagno, P. Moras, S. Vlaic, M. Etzkorn, P. M. Sheverdyaeva, D. Pacilé, H. Brune, and C. Carbone, 2010, Phys. Rev. Lett. **105**, 246803.
Schwarz, D., R. van Gastel, H. J. W. Zandvliet, and B. Poelsema, 2012, Phys. Rev. Lett. **109**, 016101.
Schwoebel, R. L., 1969, J. Appl. Phys. **40**, 614.
Šipr, O., S. Bornemann, J. Minár, and H. Ebert, 2010, Phys. Rev. B **82**, 174414.
Sutter, P., J. T. Sadowski, and E. Sutter, 2009, Phys. Rev. B **80**, 245411.
Tersoff, J., A. W. Denier van der Gon, and R. M. Tromp, 1994, Phys. Rev. Lett. **72**, 266.
Tumbek, L., C. Gleichweit, K. Zojer, and A. Winkler, 2012, Phys. Rev. B **86**, 085402.
Venables, J. A., 1973, Philos. Mag. **27**, 697.

Venables, J. A., 2000, *Introduction to Surface and Thin Film Processes* (Cambridge University Press, Cambridge, England).
Venables, J. A., G. D. T. Spiller, and M. Hanbücken, 1984, Rep. Prog. Phys. **47**, 399.
Vicsek, T., and F. Family, 1984, Phys. Rev. Lett. **52**, 1669.
Victora, R. H., and J. M. MacLaren, 1993, J. Appl. Phys. **73**, 6415.
Voloshina, E., and Y. Dedkov, 2012, Phys. Chem. Chem. Phys. **14**, 13 502.
Walton, D., 1962, J. Chem. Phys. **37**, 2182.
Wulff, G., 1901, Z. Kristallogr. New Cryst. Struct. **34**, 449.
Zangwill, A., and D. D. Vvedensky, 2011, Nano Lett. **11**, 2092.
Zeng, H., J. Li, J. P. Liu, Z. L. Wang, and S. Sun, 2002, Nature (London) **420**, 395.
Zhou, Z., F. Gao, and D. W. Goodman, 2010, Surf. Sci. **604**, L31.
Zinsmeister, G., 1966, Vacuum **16**, 529.